Air Force Institute of Technology

AFIT Scholar

3-2021

Laser Illuminated Imaging: Beam and Scene Deconvolution Algorithm

Benjamin W. Davis

LASER ILLUMINATED IMAGING: BEAM AND SCENE TRACKING DECONVOLUTION ALGORITHM

THESIS

Benjamin W. Davis, 1st Lieutenant, USSF

AFIT-ENG-MS-21-M-026

DEPARTMENT OF THE AIR FORCE
AIR UNIVERSITY

AIR FORCE INSTITUTE OF TECHNOLOGY

Wright-Patterson Air Force Base, Ohio

The views expressed in this thesis are those of the author and do not reflect the official policy or position of the United States Air Force, Department of Defense, or the United States Government. This material is declared a work of the U.S. Government and is not subject to copyright protection in the United States.

AFIT-ENG-MS-21-M-026

LASER ILLUMINATED IMAGING: BEAM AND SCENE TRACKING
DECONVOLUION ALGORITHM

THESIS

Presented to the Faculty

Department of Electrical and Computer Engineering

Graduate School of Engineering and Management

Air Force Institute of Technology

Air University

Air Education and Training Command

In Partial Fulfillment of the Requirements for the

Degree of Master of Science in Electrical Engineering

Benjamin W. Davis, BS

1st Lieutenant, USSF

March 2021

DISTRIBUTION STATEMENT A.
APPROVED FOR PUBLIC RELEASE; DISTRIBUTION UNLIMITED.

AFIT-ENG-MS-21-M-026

LASER ILLUMINATED IMAGING: BEAM AND SCENE TRACKING DECONVOLUION ALGORITHM

Benjamin W. Davis, BS
1st Lieutenant, USSF

Committee Membership:

Maj David JR Becker, PhD
Chair

Dr. Stephen C. Cain, PhD
Member

Maj Tyler J. Hardy, PhD
Member

Abstract

Laser illuminated imaging systems deal with several physical challenges that must be overcome to achieve high-resolution images of the target. Noise sources like background noise, photon counting noise, and laser speckle noise will all greatly affect the imaging system's ability to produce a high-resolution image. An even bigger challenge to laser illuminated imaging systems is atmospheric turbulence and the effect that it will have on the imaging system. The illuminating beam will experience tilt, causing the beam to wander off the center of the target during propagation. The light returning to the detector will similarly be affected by turbulence, and it too will wander off the center of the detector. The effects of tilt will be noticed in a multi-fame data set by the illuminating beam and the object shifting around the frame. This research effort uses expectation maximization to track the beam and scene motion from frame-to-frame along with a deconvolution algorithm to produce a high-resolution image of the target. Components of the expectation maximization beam and scene tracking algorithm will then be used with cross-correlation to create a hybrid algorithm to create exceptionally clear images of the target object.

Acknowledgments

I would like to express my utmost gratitude to my faculty advisor, Maj David JR Becker. His support throughout this research effort has proven invaluable, and his guidance was highly appreciated.

Benjamin W. Davis

Table of Contents

List of Figures

x

List of Tables

LASER ILLUMINATED IMAGING: BEAM AND SCENE TRACKING DECONVOLUION ALGORITHM

I. Introduction

This chapter introduces the thesis and its organization. This introduction describes the problem addressed in this thesis and its research goals. This chapter will address the assumptions taken in the research to clarify the scope of the problem. Finally, the organization structure of the thesis will be discussed.

1.1 Problem Statement

When using Laser Detection and Ranging (LADAR) systems, there are several physical challenges that must be overcome to achieve high resolution images. LADAR systems are subject to optical diffraction, atmosphere induced tilt, and laser beam speckle which all greatly impact image resolution. Tilt is found to be 87% of the imaging error [1]. The atmosphere induced tilt's influence will be realized in a multi-frame LADAR data set by causing both the beam and scene to shift around the axis of the frame. Turbulence will cause the tilt to change from frame to frame, meaning that the beam and scene will shift around the axis in each frame of a multi-frame LADAR data set.

Beyond the challenge of a shifting beam and scene in a data set, LADAR systems are subject to several noise sources that must be considered. Background noise, thermal noise, photon counting noise, and laser speckle are all prevalent in LADAR systems [2]. Each of these noise sources must be mitigated to produce a high resolution image of the target object.

This thesis proposes a post-processing algorithm that analyzes and mitigates these various challenges throughout each frame of the data set to produce a high-resolution

منارة للاستشارات

www.manaraa.com

image of the target object. The algorithm will analyze each frame of the data set and estimate the beam and scene motion independently in each frame. With this knowledge, the algorithm will perform a deconvolution to provide a clear image of the target object. The algorithm will be robust enough to handle several noise sources and produce a high-resolution image of the target object under extreme noise sources.

1.2 Research Goals

The ultimate goal of this research effort is to derive, and realize in simulation, a deconvolution algorithm to track beam and scene motion using Expectation Maximization (EM). This algorithm will estimate beam and scene shifts in each frame of a given data set and use these shift estimates to produce a high-resolution image of the target object.

1.3 Assumptions

Several assumptions were made in this research effort to limit the scope of the project:

- The shape of the long exposure Point Spread Function (PSF) is known and consistent throughout the data set
- The shape of the illuminating beam is known and consistent throughout the data set
- The target object is stationary. It is not rotating or changing scale in each frame of the data set
- The illuminating beam is small enough to limit the Field of View (FOV) of the target object

2

- The beam shifts and scene shifts are uncorrelated in time

1.4 Thesis Organization

Chapter 2 of this thesis will provide necessary background and theory to fully understand the concepts in this research effort. Chapter 3 moves into the derivation of the proposed algorithm using the EM algorithm and discusses the simulation setup to evaluate the abilities of the algorithm. Chapter 4 presents the results of the testing described earlier in Chapter 3 and analyzes these results. It compares the algorithm against the cross-correlation method and proceeds to test a hybrid algorithm with cross-correlation and EM algorithm components. Chapter 5 summarizes the results of the research effort and discusses potential follow-on research opportunities.

II. Background and Theory

This chapter touches on the background material relevant to this research effort. This section will introduce a typical LADAR system and discuss the physical challenges LADAR systems encounter. This chapter will then discuss the need for properly registered images and some commonly used image registration techniques used with LADAR systems. Finally, this section discusses deconvolution algorithms for image registration and briefly introduces the EM algorithm.

2.1 LADAR System Overview

This research will deal with a simple, generic LADAR system. The target object is illuminated with a coherent pulsed laser. This light will then reflect off the target object and return to the LADAR detector. The light will process through the LADAR optics system to produce an image of the target. This simple system is shown, below, in Figure 1.
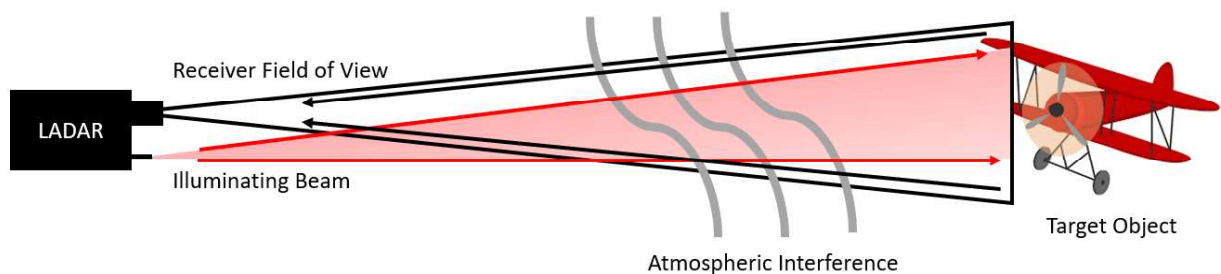
Figure 1: Generic LADAR system model

A mathematical model for the LADAR system can be written simply as a convolution of the beam and object with the PSF of the system [3]. This convolution is shown below in Equation 1. i is the intensity in the output image. The positional coordinates in the detector plane are represented by variables x and y. The positional coordinates in the target plane are represented by variables z and w. Both reference planes are considered square planes with N pixels in each direction. o represents the object, b represents the beam, and h represents the atmospheric PSF.

$$i(x,y) = \sum_{z}^{N} \sum_{w}^{N} o(z,w)b(z,w)h(x-z, y-w) \qquad 1$$

2.2 Atmospheric Turbulence

As shown in the LADAR model in Figure 1, the LADAR system will be subject to effects of atmospheric interference. Turbulence is cause by random variations in air temperature and motion that result in small changes to the refractive index of the air [4]. As light passes through these pockets of air with varying refractive indices, the light will experience phase shifts. This turbulent effect is illustrated in Figure 2.

5
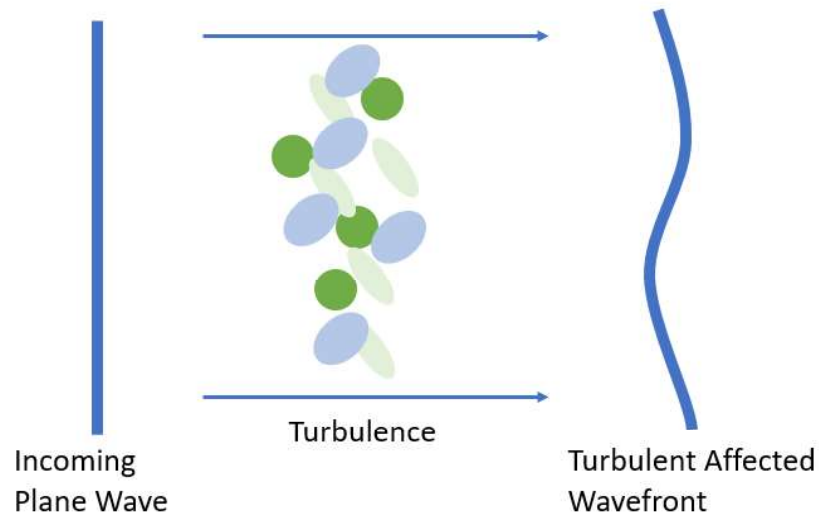
Figure 2: Effect of Atmospheric Turbulence

As mentioned earlier in Chapter 1, this research will assume that the FOV is smaller than the target; the image will show a beam limited FOV. An example of this beam limited FOV is shown below in Figure 3.
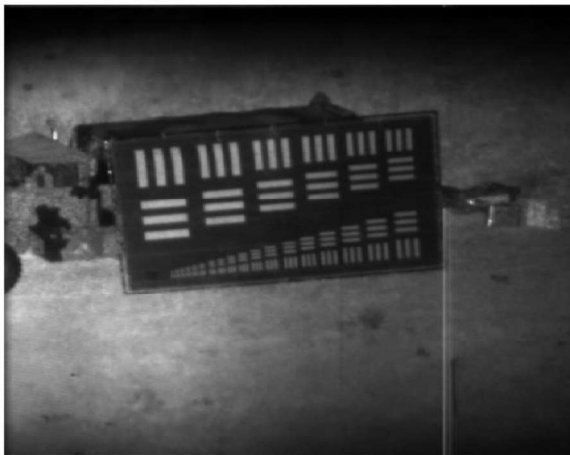
(a)   (b)

Figure 3: Original target image (a) and beam limited target (b)

6

The light will experience phase shifts as it propagates through turbulence – this phase shift will induce tilt on the beam as it propagates to the target. In the target plane, this beam tilt will make the beam shift around the target. Figure 4, below, shows an example of beam shift independent of the background scene.

(a)   (b)
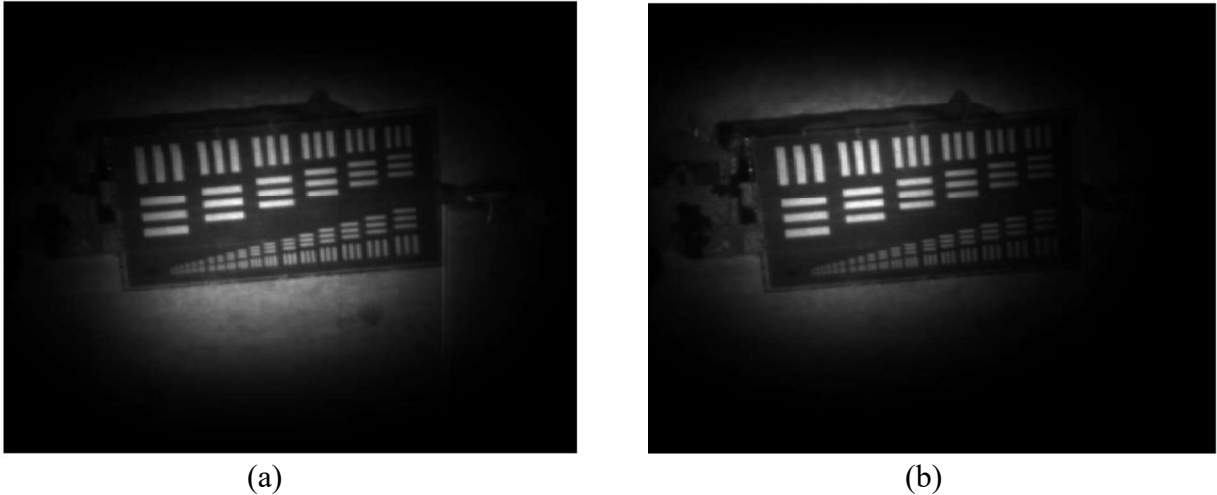
Figure 4: Beam limited target with beam shifting from frame (a) to frame (b)

These images show the beam shifting around the target while the target remains stationary in the frame. The same turbulent effect causing the beam to experience tilt will also affect the reflected light as it returns to the target; the entire scene of the image will shift around the frame. An example of a scene shift, while the beam stays fixed to the target, is simulated below in Figure 5.

7

(a)

(b)
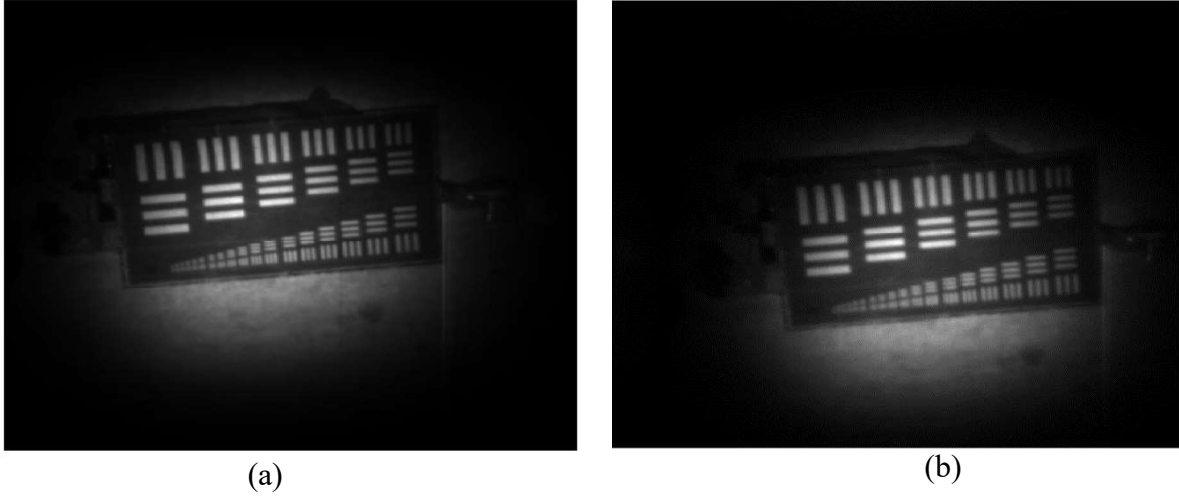
Figure 5: Beam limited target with scene shifting from frame (a) to frame (b)

These images show the beam remaining fixed to the target while the whole scene shifts around the frame. In every data set, atmospheric turbulence will cause the effects of both beam and scene shift from one frame to the next.

The tilt parameters to describe the shifts in each frame can be modeled as a zero-mean Gaussian random variable with variance described in Equation 2 [2]. σ_α^2 and σ_β^2 represent the tilt variance in a horizontal and vertical directions, respectively. D_r is the diameter of the receiver aperture and r_0 is Fried's seeing parameter. Fried's parameter is a measure of atmospheric turbulence; high values indicate weak turbulence and low values indicate strong turbulence.

$$\sigma_\alpha^2 = \sigma_\beta^2 = 0.448 \left(\frac{D_r}{r_0}\right)^{5/3} \qquad 2$$

Equation 2 implies that higher values of Fried's seeing parameter – representing weak turbulence – will result in lower tilt variance. Likewise, low values for Fried's parameter will result in greater shift variance.

8

Returning to Equation 1 for the mathematical model for the LADAR system, the model can be updated to include atmosphere induced beam shifts or scene shifts [3]. This new equation is shown below in Equation 3. This equation now deals with a data set consisting of multiple image frames. i_k is the intensity image in the kth frame. γ_k and ε_k are the beam shift parameters for the kth frame in the x and y directions, respectively. α_k and β_k are the scene shift parameters for the kth frame in the x and y directions, respectively.

$$i_k(x,y) = \sum_{z}^{N} \sum_{w}^{N} o(z,w)\, b(z - \gamma_k, w - \varepsilon_k) h(x - z - \alpha_k, y - w - \beta_k) \qquad 3$$

2.3 Noise Considerations

LADAR systems deal with several significant noise sources: background noise, thermal noise, photon counting noise, and laser speckle [5]. These noise sources will decrease the Signal-to-Noise Ratio (SNR) and hurt overall performance of a LADAR system.

Background noise is any kind of light collected by the detector that isn't reflected laser light off the target [2]. Light sources that contribute to background noise could be sunlight, moonlight, light reflecting off other surfaces towards the detector, and any other number of sources. An effective way to estimate the background noise collected in a LADAR system is to take images with the illuminating source turned off. The background noise can then be estimated using the median value of the intensity collected

9

at the detector. Using this estimated level of background noise, this noise source can be counteracted.

Thermal noise is present in the system because anything above 0 K will radiate photons. The room temperature CCD will radiate photons, and these photons will interfere with the detector creating noise [2]. These photons can induce current in the circuitry which will create read-out noise. The amount of thermal noise present can be practically measured by measuring the dark current in the system – the current running through the detector with the shutter closed.

Photon counting noise is present in the LADAR system due to the fact that photons arrive at random times [2]. Photo-electrons counted in a CCD integration time is known to be a random variable with mean proportional to the expected value. The number of photons measured at the detector has been proven to be a Poisson random variable. Using this knowledge, the Poisson counting noise can also be measured to account for noise. Equation 4, below, gives the Probability Mass Function (PMF) for a Poisson random variable. r is the photons counted in a given pixel and λ is the mean number of photons arriving in the time interval.

$$P(r) = \frac{\lambda^r e^{-\lambda}}{r!} \qquad 4$$

The most impactful noise source that LADAR systems must address is laser speckle. Laser speckle is a product of a coherent light source reflecting off of a rough surface – rough relative to the light's wavelength [6]. Figure 6 shows how this phenomenon occurs.

10
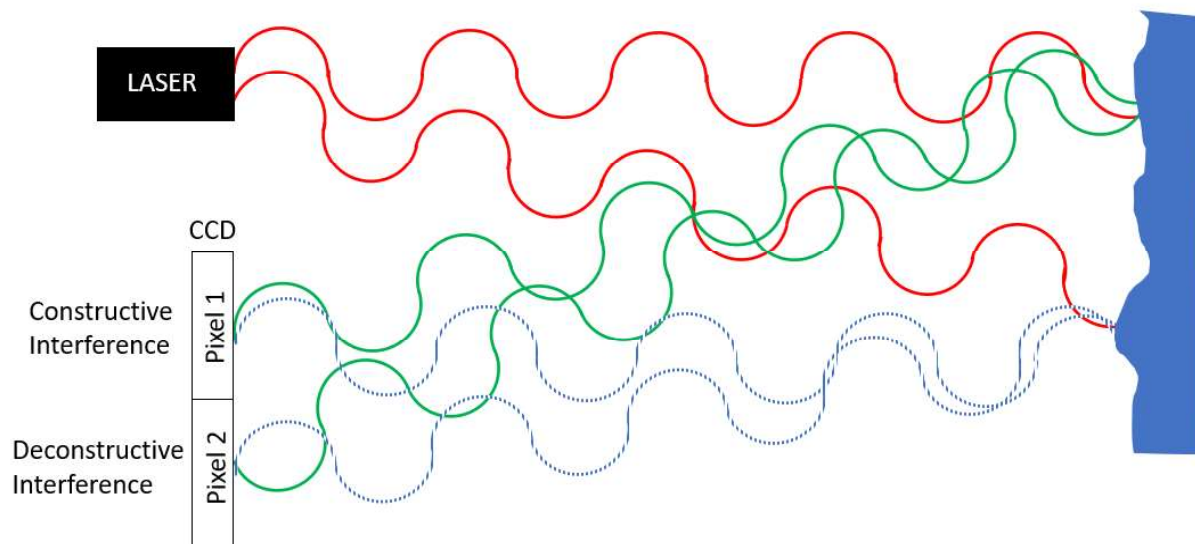
Figure 6: Laser speckle constructive (CCD pixel 1) and deconstructive interference (CCD pixel 2)

The red waves emanating from the laser hit the object and reflect back to the detector. The waves reflecting off the object returning to the CCD are shown in green and blue dashes. The waves travel different distances, meaning that they do not arrive at the CCD in phase. Some waves will arrive in phase and produce constructive interference, as shown in Pixel 1 in Figure 6. Some waves will arrive out of phase and produce deconstructive interference, as shown in Pixel 2 in Figure 6. These varying points of constructive and deconstructive interference will produce randomly dispersed bright and dark spots throughout the image [6]. This granular appearance in the image is known as laser speckle. Figure 7, below, shows a simulated beam limited image with and without laser speckle added.

11
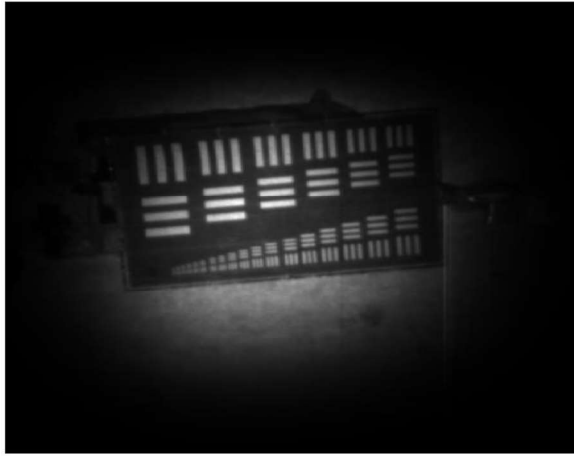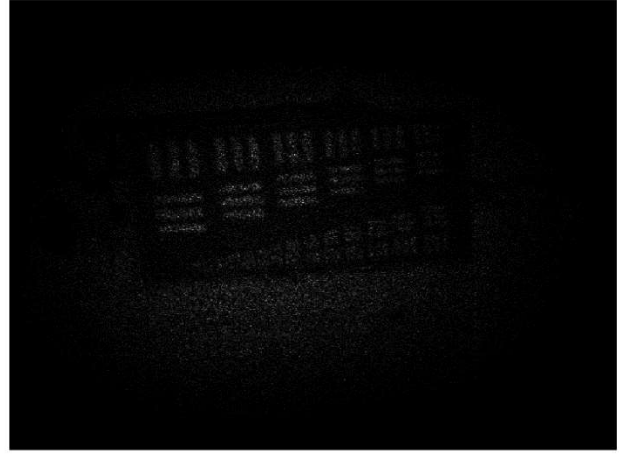
(a)   (b)

Figure 7: Beam limited target with (b) and without (a) laser speckle

The intensity peaks in laser speckle are known to follow a gamma distribution [5]. When this gamma laser speckle effect is combined with the Poisson effect from photon counting, the resulting effect follows a negative binomial distribution. This can be simulated as a negative binomial random variable with mean of $E[N_{Signal}]$ and variance, $\sigma^2{}_{speckle}$, calculated in Equation 5, below. M is the coherency factor of the light. A coherency factor of one means the light is fully coherent, and a coherency factor of infinity means the light is fully incoherent.

$$\sigma^2{}_{speckle} = E[N_{Signal}]\left(1 + \frac{E[N_{Signal}]}{M}\right) \qquad 5$$

2.4 Image Registration

Looking at Figure 7, it is clear that LADAR system images will need image registration to produce a clean output image. One successful method for dealing with a data set obscured by laser speckle is to collect multiple frames of data and average across

12

the frames. If multiple frames can be aligned properly, averaging across these frames produces high resolution images. Figure 8, below, shows the result of averaging across 10 and 100 perfectly aligned frames in in (a) and (b) respectively.

(a)   (b)
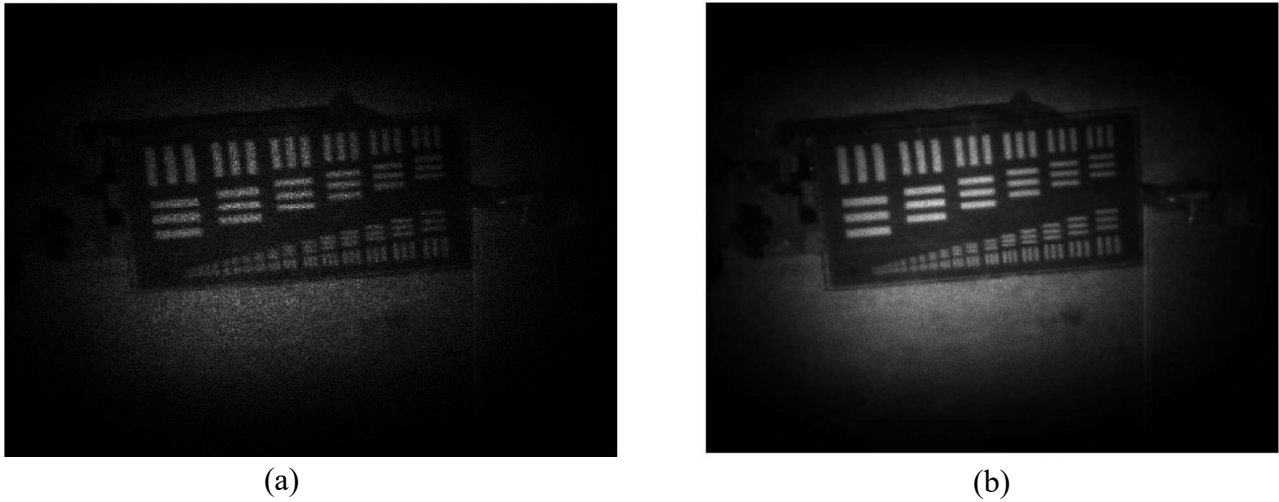
Figure 8: Averaging across 10 frames (a) and 100 frames (b)

Averaging across 10 frames shows some effects of the speckle but shows the target with some clarity. Averaging across 100 frames appears to completely remove the effect of noise. This figure illustrates that averaging across perfectly aligned frames produces high quality images and averaging across more frames will produce a higher resolution image.

If the frames are not properly aligned, the grainy appearance from the speckle will reduce, but the resulting image will not result in a high-resolution image. Figure 9 shows the result of averaging across 10 perfectly aligned frames and 10 misaligned frames. The average across misaligned frames is very blurry in comparison to the average across perfectly aligned frames.

<center>(a)</center> <center>(b)</center>
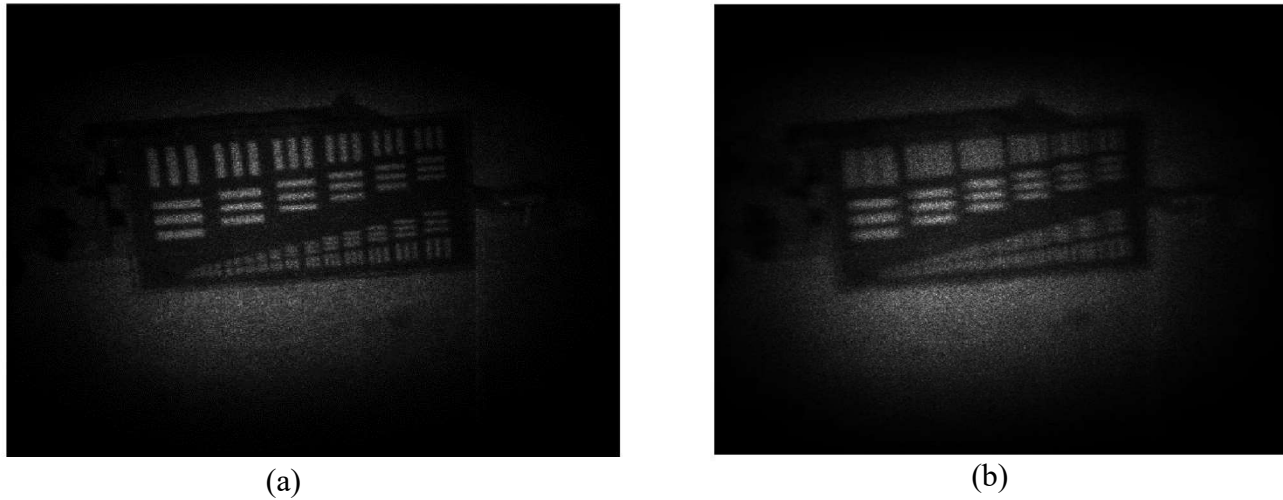
Figure 9: Averaging 10 properly aligned frames (a) and 10 misaligned frames (b)

Figure 9 demonstrates that proper image registration with each frame of data is essential in producing a high-resolution output image.

One established method used in image registration is cross-correlation [7]. Cross-correlation is a method that takes the correlation between two images. The maximum point in the normalized correlation gives the estimated shifts in the x and y directions between the two images. Using this method, multiple frames can be aligned properly to average across. This technique will be used as a comparison point against the algorithm derived in this research.

2.5 Expectation Maximization

Expectation Maximization (EM) is an iterative method to compute the maximum likelihood estimate of a mathematical model [8]. This research will utilize the EM algorithm with the mathematical model shown in Equation 3 to estimate the likeliest

<center>14</center>

shifts in the beam and scene. The EM algorithm is a seven-step process that leverages some statistical nature of the mathematical model to create a Bayesian estimator. This research will leverage the Poisson nature of light to create the estimator. Using this iterative EM algorithm, a deconvolution algorithm will be derived to increase resolution of the target object. The Ayers-Dainty blind deconvolution algorithm [9] and the multi-frame blind deconvolution (MFBD) algorithm [10] are discussed in depth. In blind deconvolution algorithms, both the object and the optical system's OTF is estimated. This research differs from these algorithms in that the optical system's OTF is known; only the object needs estimated in this research. These algorithms, however, do not track beam motion which this research will do.

15

This section provides the derivation of the beam and scene tracking deconvolution algorithm. This section will walk through the steps of the EM process to derive the update equations for the beam and scene tracking algorithm. Once the algorithm has been derived, this section will continue into testing methods to validate the approach.

3.1 Algorithm Derivation

The beam and scene tracking deconvolution algorithm relies on EM to derive the key components to build the algorithm. EM provides a seven-step method to create Bayesian Estimators to solve many-to-one mapping problems.

3.1.1 EM Algorithm Step 1

Obtain statistical model for your measured data (called incomplete data). The incomplete data, d_k, is the measurable data collected by the detector. The expected value of the incomplete data, shown in Equation 6, can be represented mathematically as a convolution of the beam multiplied object and the PSF. The shift parameters are the same as previously defined in Equation 3.

$$E[d_k(x,y)] = \sum_z^N \sum_w^N o(z,w)b(z-\gamma_k, w-\varepsilon_k)h(x-z-\alpha_k, y-w-\beta_k) \qquad 6$$

3.1.2 EM Algorithm Step 2

Invent a set of mythical data (called complete data) and a relationship between this data and the incomplete data. The expected value of the complete data, $\tilde{d}_k$, is defined below in Equation 7. This is the invented data set that will be used later to solve for the estimate for the incomplete data.

$$E\left[\tilde{d}_k(x,y,z,w)\right] = o(z,w)b(z-\gamma_k, w-\varepsilon_k)h(x-z-\alpha_k, y-w-\beta_k) \qquad 7$$

3.1.3 EM Algorithm Step 3

Select a statistical model for the complete data so that it produces the statistical model for the incomplete data through their pre-defined relationship. The incomplete data is now defined as the double sum over all z and w of the complete data, shown in Equation 8.

$$d_k(x,y) = \sum_z^N \sum_w^N \tilde{d}_k(x,y,z,w) \qquad 8$$

3.1.4 EM Algorithm Step 4

Formulate the complete data log-likelihood. Leveraging the Poisson nature of light, the log-likelihood is shown below as the natural log of the Poisson PMF of the complete data. The PMF of the complete data is shown below in Equation 9. The mean of the complete data was defined previously in Equation 7 and is used in the Poisson PMF.

$$P\left(\tilde{d}_k(x,y,z,w)\right) \qquad 9$$

$$= \frac{o(z,w)b(z-\gamma_k, w-\varepsilon_k)h(x-z-\alpha_k, y-w-\beta_k)^{\tilde{d}_k(x,y,z,w)} e^{-o(z,w)b(z-\gamma_k,w-\varepsilon_k)h(x-z-\alpha_k,y-w-\beta_k)}}{\tilde{d}_k(x,y,z,w)!}$$

Solving for all pixels, x and y, across all frames, k, gives the joint probability of all pixels and all frames to be used for the log-likelihood. Because each pixel and frame are statistically independent of each other, the joint probability can be written as the product of each individual PMF. Therefore, the joint probability is the product over $k, x, y, z,$ and w of Equation 9. This joint PMF is shown in Equation 10.

17

$$P\big(\tilde{d}_k(x,y,z,w)\ \forall\ x,y,z,w\big) = \tag{10}$$

$$\prod_k^K \prod_x^N \prod_y^N \prod_z^N \prod_w^N \frac{o(z,w)b(z-\gamma_k,w-\varepsilon_k)h(x-z-\alpha_k,y-w-\beta_k)^{\tilde{d}_k(x,y,z,w)} e^{-o(z,w)b(z-\gamma_k,w-\varepsilon_k)h(x-z-\alpha_k,y-w-\beta_k)}}{\tilde{d}_k(x,y,z,w)!}$$

Now, the natural logarithm of Equation 10 is taken, giving the complete data log-likelihood, $L(o,a_k,\beta_k,\gamma_k,\epsilon_k)$, defined below in Equation 11.

$$L(o,a_k,\beta_k,\gamma_k,\epsilon_k) \tag{11}$$

$$= \sum_k^K \sum_x^N \sum_y^N \sum_z^N \sum_w^N \tilde{d}_k(x,y,z,w)\ln\big(o(z,w)b(z-\gamma_k,w-\varepsilon_k)h(x-z-\alpha_k,y-w-\beta_k)\big)$$

$$-o(z,w)b(z-\gamma_k,w-\varepsilon_k)h(x-z-\alpha_k,y-w-\beta_k)-\ln(\tilde{d}_k(x,y,z,w)!)$$

The product operators in Equation 10 are now summation operators once the natural logarithm is taken, making the resulting equation much simpler to solve.

3.1.5 EM Algorithm Step 5

Compute the conditional expected value of the complete data log-likelihood given the incomplete data and old estimates of the parameters you are trying to estimate. Because the expectation operator is a linear operator, the conditional expectation of the log-likelihood can be separated into three separate terms. This conditional expectation is expanded in Equation 12.

$$E\big[L(o,a_k,\beta_k,\gamma_k,\epsilon_k)\big|o^{old},a_k^{old},\beta_k^{old},\gamma_k^{old},\varepsilon_k^{old}\big] \tag{12}$$

$$= \sum_k^K \sum_x^N \sum_y^N \sum_z^N \sum_w^N E\Big[\tilde{d}_k(x,y,z,w)\ln\big(o(z,w)b(z-\gamma_k,w-\varepsilon_k)h(x-z-\alpha_k,y-w$$

$$-\beta_k)\big)\big|o^{old},a_k^{old},\beta_k^{old},\gamma_k^{old},\varepsilon_k^{old}\Big]$$

$$-E\big[o(z,w)b(z-\gamma_k,w-\varepsilon_k)h(x-z-\alpha_k,y-w-\beta_k)\big|o^{old},a_k^{old},\beta_k^{old},\gamma_k^{old},\varepsilon_k^{old}\big]$$

$$-E\Big[\ln(\tilde{d}_k(x,y,z,w)!)\big|o^{old},a_k^{old},\beta_k^{old},\gamma_k^{old},\varepsilon_k^{old}\Big]$$

Each separate conditional expectation term in Equation 12 will be simplified individually before being recombined to form the total conditional expectation.

First Term: Because the natural logarithm of the object, beam, and PSF are constants, they can be pulled outside of the expectation operator. This results in Equation 13 below.

$$\mathrm{E}\big[\tilde{d}_k(x,y,z,w)\ln\big(o(z,w)b(z-\gamma_k,w-\varepsilon_k)h(x-z-\alpha_k,y-w-\beta_k)\big)\,|\,o^{old},a_k^{old},\beta_k^{old},\gamma_k^{old},\varepsilon_k^{old}\big] \tag{13}$$

$$= \mathrm{E}\big[\tilde{d}_k(x,y,z,w)\,|\,o^{old},a_k^{old},\beta_k^{old},\gamma_k^{old},\varepsilon_k^{old}\big]\ln\big(o(z,w)b(z-\gamma_k,w-\varepsilon_k)h(x-z-\alpha_k,y-w-\beta_k)\big)$$

The derivation of the conditional expectation of the complete data is shown in Appendix A. The solution of this expectation is shown in Equation 14 below.

$$\mathrm{E}\big[\tilde{d}_k(x,y,z,w)\,|\,o^{old},a_k^{old},\beta_k^{old},\gamma_k^{old},\varepsilon_k^{old}\big] = \tag{14}$$

$$\frac{o^{old}b(z-\gamma_k{}^{old},w-\varepsilon_k{}^{old})h\big(x-z-\alpha_k{}^{old},y-w-\beta_k{}^{old}\big)d_k(x,y)}{\sum_z^N\sum_w^N o^{old}b(z-\gamma_k^{old},w-\varepsilon_k^{old})h\big(x-z-a_k^{old},y-w-\beta_k^{old}\big)}$$

Substituting Equation 14 into Equation 13, the solution to the first term is shown below in Equation 15.

$$\mathrm{E}\big[\tilde{d}_k(x,y,z,w)\ln\big(o(z,w)b(z-\gamma_k,w-\varepsilon_k)h(x-z-\alpha_k,y-w-\beta_k)\big)\,|\,o^{old},a_k^{old},\beta_k^{old},\gamma_k^{old},\varepsilon_k^{old}\big] \tag{15}$$

$$= \frac{o^{old}b\big(z-\gamma_k{}^{old},w-\varepsilon_k{}^{old}\big)h\big(x-z-\alpha_k{}^{old},y-w-\beta_k{}^{old}\big)d_k(x,y)}{\sum_z^N\sum_w^N o^{old}b\big(z-\gamma_k^{old},w-\varepsilon_k^{old}\big)h\big(x-z-a_k^{old},y-w-\beta_k^{old}\big)}\ln\big(o(z,w)b(z$$

$$-\gamma_k,w-\varepsilon_k)h(x-z-\alpha_k,y-w-\beta_k)\big)$$

Second Term: The object, beam, and PSF are constants, so the expected value of the second term is simply the product of the object, the beam, and the PSF. This is shown in Equation 16.

$$\mathrm{E}\big[o(z,w)b(z-\gamma_k,w-\varepsilon_k)h(x-z-\alpha_k,y-w-\beta_k)\,|\,o^{old},a_k^{old},\beta_k^{old},\gamma_k^{old},\varepsilon_k^{old}\big] \tag{16}$$

$$= o(z,w)b(z-\gamma_k,w-\varepsilon_k)h(x-z-\alpha_k,y-w-\beta_k)$$

Third Term:

19

$$\text{E}[\ln\big(\tilde{d}_k(x,y,z,w)!\big)|o^{old}, a_k^{old}, \beta_k^{old}, \gamma_k^{old}, \varepsilon_k^{old}]$$

 This term can be ignored in the expectation maximization because it will not vary with respect to the unknown parameters and will not have any effect on the maximization. Ignoring this third term saves unnecessary computations in the algorithm and speeds up the algorithm. The total conditional expectation, Equation 18, can now be written by summing Equation 15 and Equation 16.

Total Conditional Expectation of the Complete Data Log-Likelihood:

$$E[L(o, a_k, \beta_k, \gamma_k, \epsilon_k)|o^{old}, a_k^{old}, \beta_k^{old}, \gamma_k^{old}, \varepsilon_k^{old}]$$

18

$$= \sum_k^K \sum_x^N \sum_y^N \sum_z^N \sum_w^N \frac{o^{old} b(z - \gamma_k^{old}, w - \varepsilon_k^{old}) h(x - z - \alpha_k^{old}, y - w - \beta_k^{old}) d_k(x,y)}{\sum_z^N \sum_w^N o^{old} b(z - \gamma_k^{old}, w - \varepsilon_k^{old}) h(x - z - a_k^{old}, y - w - \beta_k^{old})} \ln(o(z,w)b(z$$

$$-\gamma_k, w - \varepsilon_k)\, h(x - z - \alpha_k, y - w - \beta_k)) - o(z,w) b(z - \gamma_k, w - \varepsilon_k) h(x - z - \alpha_k, y - w - \beta_k)$$

3.1.6 EM Algorithm Step 6

Maximize the conditional expected value of the complete data log-likelihood with respect to the parameters you are trying to estimate. The three parameters being estimated are the target object, the beam shifting parameters, and the scene shifting parameters.

Maximize Target Object: To maximize the target, the derivative of Equation 18 is taken with respect to a single point of the object, $o(z_o, w_o)$. This step is shown in Equation 19.

$$\frac{\partial}{\partial o(z_0, w_o)} E\left[L\left(o, a_k, \beta_k, \gamma_k, \epsilon_k\right)\big|o^{old}, a_k^{old}, \beta_k^{old}, \gamma_k^{old}, \varepsilon_k^{old}\right] =$$

19

$$\sum_k^K \sum_x^N \sum_y^N \sum_z^N \sum_w^N \frac{\partial}{\partial o(z_0, w_o)} \frac{o^{old} b\big(z - \gamma_k^{old}, w - \varepsilon_k^{old}\big) h\big(x - z - \alpha_k^{old}, y - w - \beta_k^{old}\big) d_k(x,y)}{\sum_z^N \sum_w^N o^{old} b\big(z - \gamma_k^{old}, w - \varepsilon_k^{old}\big) h\big(x - z - a_k^{old}, y - w - \beta_k^{old}\big)} \ln\big(o(z,w)b(z - \gamma_k, w$$

$$-\varepsilon_k) h(x - z - \alpha_k, y - w - \beta_k)) - \frac{\partial}{\partial o(z_0, w_o)}\, o(z,w) b(z - \gamma_k, w - \varepsilon_k) h(x - z - \alpha_k, y - w - \beta_k)$$

$$= \sum_k^K \sum_x^N \sum_y^N \sum_z^N \sum_w^N \frac{o^{old} b\big(z - \gamma_k^{old}, w - \varepsilon_k^{old}\big) h\big(x - z - \alpha_k^{old}, y - w - \beta_k^{old}\big) d_k(x,y)}{\sum_z^N \sum_w^N o^{old} b\big(z - \gamma_k^{old}, w - \varepsilon_k^{old}\big) h\big(x - z - a_k^{old}, y - w - \beta_k^{old}\big)} \frac{1}{o(z,w)} \delta(z - z_o, w$$

$$- w_o) - b(z - \gamma_k, w - \varepsilon_k) h(x - z - \alpha_k, y - w - \beta_k) \delta(z - z_o, w - w_o)$$

The Dirac functions were introduced because the derivative is being taken with respect to the single point, (z_0, w_o). The derivative will be zero anywhere where z does not equal z_0 or w does not equal w_o. The summations over z and w can be dropped due to the sifting property of the Dirac delta function. These simplifications result in Equation 20.

$$\frac{\partial}{\partial o(z_0, w_o)} E\left[L\left(o, a_k, \beta_k, \gamma_k, \epsilon_k\right) \big| o^{old}, a_k^{old}, \beta_k^{old}, \gamma_k^{old}, \varepsilon_k^{old}\right] =$$

$$\sum_k^K \sum_x^N \sum_y^N \frac{o^{old} b(z - {\gamma_k}^{old}, w - {\varepsilon_k}^{old}) h\left(x - z - {\alpha_k}^{old}, y - w - {\beta_k}^{old}\right) d_k(x, y)}{\sum_z^N \sum_w^N o^{old} b\left(z - \gamma_k^{old}, w - \varepsilon_k^{old}\right) h\left(x - z - a_k^{old}, y - w - \beta_k^{old}\right)} \frac{1}{o(z_0, w_o)} \quad 20$$

$$- b(z_0 - \gamma_k, w_o - \varepsilon_k) h(x - z_0 - \alpha_k, y - w_o - \beta_k)$$

Now, setting Equation 20 equal to zero and solving for $o(z_0, w_o)$, the maximized object can be found in Equations 21 - 23.

$$\sum_k^K \sum_x^N \sum_y^N \frac{o^{old} b(z - {\gamma_k}^{old}, w - {\varepsilon_k}^{old}) h\left(x - z - {\alpha_k}^{old}, y - w - {\beta_k}^{old}\right) d_k(x, y)}{\sum_z^N \sum_w^N o^{old} b\left(z - \gamma_k^{old}, w - \varepsilon_k^{old}\right) h\left(x - z - a_k^{old}, y - w - \beta_k^{old}\right)} \frac{1}{o(z_0, w_o)} \quad 21$$

$$- \sum_k^K \sum_x^N \sum_y^N b(z_0 - \gamma_k, w_o - \varepsilon_k) h(x - z_0 - \alpha_k, y - w_o - \beta_k) = 0$$

$$\sum_k^K \sum_x^N \sum_y^N b(z_0 - \gamma_k, w_o - \varepsilon_k) h(x - z_0 - \alpha_k, y - w_o - \beta_k) = \quad 22$$

$$\sum_k^K \sum_x^N \sum_y^N \frac{o^{old} b(z - {\gamma_k}^{old}, w - {\varepsilon_k}^{old}) h\left(x - z - {\alpha_k}^{old}, y - w - {\beta_k}^{old}\right) d_k(x, y)}{\sum_z^N \sum_w^N o^{old} b\left(z - \gamma_k^{old}, w - \varepsilon_k^{old}\right) h\left(x - z - a_k^{old}, y - w - \beta_k^{old}\right)} \frac{1}{o(z_0, w_o)}$$

$$o(z_0, w_o)$$

$$= \frac{\sum_k^K \sum_x^N \sum_y^N \frac{o^{old} b(z - \gamma_k^{old}, w - \varepsilon_k^{old}) h(x - z - \alpha_k^{old}, y - w - \beta_k^{old}) d_k(x,y)}{\sum_z^N \sum_w^N o^{old} b(z - \gamma_k^{old}, w - \varepsilon_k^{old}) h(x - z - a_k^{old}, y - w - \beta_k^{old})}}{\sum_k^K \sum_x^N \sum_y^N b(z_0 - \gamma_k, w_o - \varepsilon_k) h(x - z_0 - \alpha_k, y - w_o - \beta_k)}$$

Finally, leveraging that the sum over x and y of the PSF is one, the PSF and summations can be dropped from the denominator. This gives the target object update equation below in Equation 24.

$$o(z_0, w_o)$$

24

$$= \frac{\sum_k^K \sum_x^N \sum_y^N \frac{o^{old} b(z - \gamma_k^{old}, w - \varepsilon_k^{old}) h(x - z - \alpha_k^{old}, y - w - \beta_k^{old}) d_k(x,y)}{\sum_z^N \sum_w^N o^{old} b(z - \gamma_k^{old}, w - \varepsilon_k^{old}) h(x - z - a_k^{old}, y - w - \beta_k^{old})}}{\sum_k^K b(z_0 - \gamma_k, w_o - \varepsilon_k)}$$

Maximize Beam Shift: Returning to the total conditional expectation in Equation 18, the logarithm of the product of the object, beam, and scene can be separated into the sum of three logarithms. This step is shown in Equation 25.

$$E\big[L\big(o, a_k, \beta_k, \gamma_k, \epsilon_k\big)\big|o^{old}, a_k^{old}, \beta_k^{old}, \gamma_k^{old}, \varepsilon_k^{old}\big] =$$

$$\sum_k^K \sum_x^N \sum_y^N \sum_z^N \sum_w^N \frac{o^{old} b(z - \gamma_k^{old}, w - \varepsilon_k^{old}) h(x - z - \alpha_k^{old}, y - w - \beta_k^{old}) d_k(x,y)}{\sum_z^N \sum_w^N o^{old} b(z - \gamma_k^{old}, w - \varepsilon_k^{old}) h(x - z - a_k^{old}, y - w - \beta_k^{old})} \big(ln\,(o(z,w))$$

25

$$+ \ln\big(b(z - \gamma_k, w - \varepsilon_k)\big) + \ln(h(x - z - \alpha_k, y - w - \beta_k)))$$

$$- o(z,w) b(z - \gamma_k, w - \varepsilon_k) h(x - z - \alpha_k, y - w - \beta_k)$$

Any term that does not vary with respect to the beam shift parameters, γ_k and ε_k, can be ignored. Because they do not vary with our parameters of interest, they will have no impact on maximizing the equation. They will be constant across each realization of the equation as the shift parameters vary and can effectively be ignored. The logarithms of

the object and the PSF, highlighted in Equation 26, fill these requirements and will be removed from the equation.

$$E[L(o, a_k, \beta_k, \gamma_k, \epsilon_k)|o^{old}, a_k^{old}, \beta_k^{old}, \gamma_k^{old}, \varepsilon_k^{old}]$$

$$= \sum_k^K \sum_x^N \sum_y^N \sum_z^N \sum_w^N \frac{o^{old} b\left(z - \gamma_k^{old}, w - \varepsilon_k^{old}\right) h\left(x - z - \alpha_k^{old}, y - w - \beta_k^{old}\right) d_k(x, y)}{\sum_z^N \sum_w^N o^{old} b\left(z - \gamma_k^{old}, w - \varepsilon_k^{old}\right) h\left(x - z - \alpha_k^{old}, y - w - \beta_k^{old}\right)} \left(\boxed{\ln(o(z, w))}\right. \qquad 26$$

$$\left. + \ln\left(b(z - \gamma_k, w - \varepsilon_k)\right) + \boxed{\ln\left(h(x - z - \alpha_k, y - w - \beta_k)\right)}\right)$$

$$- o(z, w) b(z - \gamma_k, w - \varepsilon_k) h(x - z - \alpha_k, y - w - \beta_k)$$

Removing the two unneeded logarithms in Equation 26 and expanding the second term into a separate summation gives the proportional equation below, Equation 27.

$$\propto \sum_k^K \sum_x^N \sum_y^N \sum_z^N \sum_w^N \frac{o^{old} b\left(z - \gamma_k^{old}, w - \varepsilon_k^{old}\right) h\left(x - z - \alpha_k^{old}, y - w - \beta_k^{old}\right) d_k(x, y)}{\sum_z^N \sum_w^N o^{old} b\left(z - \gamma_k^{old}, w - \varepsilon_k^{old}\right) h\left(x - z - \alpha_k^{old}, y - w - \beta_k^{old}\right)} \ln\left(b(z - \gamma_k, w - \varepsilon_k)\right) \qquad 27$$

$$- \sum_k^K \sum_x^N \sum_y^N \sum_z^N \sum_w^N o(z, w) b(z - \gamma_k, w - \varepsilon_k) h(x - z - \alpha_k, y - w - \beta_k)$$

And finally, leveraging again that the sum over x and y of the PSF is one, the PSF and summations can be dropped from the second term. This results in the beam shift maximization equation below, Equation 28. Q_B is the conditional expectation of the beam shift equation.

$$Q_B(\gamma_k, \varepsilon_k)$$

$$= \sum_k^K \sum_x^N \sum_y^N \sum_z^N \sum_w^N \frac{o^{old} b\left(z - \gamma_k^{old}, w - \varepsilon_k^{old}\right) h\left(x - z - \alpha_k^{old}, y - w - \beta_k^{old}\right) d_k(x, y)}{\sum_z^N \sum_w^N o^{old} b\left(z - \gamma_k^{old}, w - \varepsilon_k^{old}\right) h\left(x - z - \alpha_k^{old}, y - w - \beta_k^{old}\right)} \ln\left(b(z - \gamma_k, w - \varepsilon_k)\right) \qquad 28$$

$$- \sum_k^K \sum_z^N \sum_w^N o(z, w) b(z - \gamma_k, w - \varepsilon_k)$$

The expectation is calculated over a range of γ_k and ε_k, and the combination of γ_k and ε_k that maximizes the expectation of the beam shift is chosen.

Maximize Scene Shift: The derivation of the scene shift maximization equation is very similar to that of the beam shift maximization equation. This derivation will return again to Equation 25, shown again below. Any term that does not vary with respect to the scene shift parameters, α_k and β_k can be ignored.

$$E[L(o, a_k, \beta_k, \gamma_k, \epsilon_k)|o^{old}, a_k^{old}, \beta_k^{old}, \gamma_k^{old}, \varepsilon_k^{old}]$$

$$= \sum_k^K \sum_x^N \sum_y^N \sum_z^N \sum_w^N \frac{o^{old} b(z - \gamma_k{}^{old}, w - \varepsilon_k{}^{old}) h(x - z - \alpha_k{}^{old}, y - w - \beta_k{}^{old}) d_k(x, y)}{\sum_z^N \sum_w^N o^{old} b(z - \gamma_k{}^{old}, w - \varepsilon_k{}^{old}) h(x - z - a_k^{old}, y - w - \beta_k^{old})} (ln\,(o(z, w)) \qquad 25$$

$$+ \ln(b(z - \gamma_k, w - \varepsilon_k)) + \ln(h(x - z - \alpha_k, y - w - \beta_k))$$

$$- o(z, w) b(z - \gamma_k, w - \varepsilon_k) h(x - z - \alpha_k, y - w - \beta_k)$$

Any term that does not vary with respect to the scene shift parameters, α_k and β_k, can be ignored. The logarithms of the object and the beam fill these requirements and will be removed from the equation. This step in shown in Equation 29.

$$E[L(o, a_k, \beta_k, \gamma_k, \epsilon_k)|o^{old}, a_k^{old}, \beta_k^{old}, \gamma_k^{old}, \varepsilon_k^{old}]$$

$$= \sum_k^K \sum_x^N \sum_y^N \sum_z^N \sum_w^N \frac{o^{old} b(z - \gamma_k{}^{old}, w - \varepsilon_k{}^{old}) h(x - z - \alpha_k{}^{old}, y - w - \beta_k{}^{old}) d_k(x, y)}{\sum_z^N \sum_w^N o^{old} b(z - \gamma_k{}^{old}, w - \varepsilon_k{}^{old}) h(x - z - a_k^{old}, y - w - \beta_k^{old})} (\,\boxed{ln\,(o(z, w)} \qquad 29$$

$$+ \boxed{\ln(b(z - \gamma_k, w - \varepsilon_k))} + \ln(h(x - z - \alpha_k, y - w - \beta_k)))$$

$$- o(z, w) b(z - \gamma_k, w - \varepsilon_k) h(x - z - \alpha_k, y - w - \beta_k)$$

Removing the two unneeded terms and expanding the second term into a separate summation gives the proportional equation below, Equation 30.

$$\propto \sum_k^K \sum_x^N \sum_y^N \sum_z^N \sum_w^N \frac{o^{old}b(z-\gamma_k{}^{old},w-\varepsilon_k{}^{old})h(x-z-\alpha_k{}^{old},y-w-\beta_k{}^{old})d_k(x,y)}{\sum_z^N \sum_w^N o^{old}b(z-\gamma_k^{old},w-\varepsilon_k^{old})h(x-z-a_k^{old},y-w-\beta_k^{old})} \ln\big(h(x-z-\alpha_k,y-w-\beta_k)\big) \qquad 30$$

$$-\sum_k^K \sum_x^N \sum_y^N \sum_z^N \sum_w^N o(z,w)b(z-\gamma_k,w-\varepsilon_k)h(x-z-\alpha_k,y-w-\beta_k)$$

Leveraging again that the sum over x and y of the PSF is one, the PSF and summations over x and y can be dropped from the second term. This leaves a summation over k, w, and z of the object and beam; however, this does not vary with the scene shift parameters and can be ignored completely, as highlighted in Equation 31.

$$\propto \sum_k^K \sum_x^N \sum_y^N \sum_z^N \sum_w^N \frac{o^{old}b(z-\gamma_k{}^{old},w-\varepsilon_k{}^{old})h(x-z-\alpha_k{}^{old},y-w-\beta_k{}^{old})d_k(x,y)}{\sum_z^N \sum_w^N o^{old}b(z-\gamma_k^{old},w-\varepsilon_k^{old})h(x-z-a_k^{old},y-w-\beta_k^{old})} \ln(h(x \qquad 31$$

$$-z-\alpha_k,y-w-\beta_k)) \; -\underbrace{\sum_k^K \sum_z^N \sum_w^N o(z,w)b(z-\gamma_k,w-\varepsilon_k)}$$

The resulting equation, Equation 32, is the final scene shift maximization equation. Q_S is the conditional expectation of the scene shift equation.

$$Q_S(\alpha_k,\beta_k)$$

$$= \sum_k^K \sum_x^N \sum_y^N \sum_z^N \sum_w^N \frac{o^{old}b(z-\gamma_k^{old},w-\varepsilon_k^{old})h(x-z-a_k^{old},y-w-\beta_k^{old})d_k(x,y)}{\sum_z^N \sum_w^N o^{old}b(z-\gamma_k^{old},w-\varepsilon_k^{old})h(x-z-a_k^{old},y-w-\beta_k^{old})} \ln\big(h(x-z-\alpha_k,y-w-\beta_k)\big) \qquad 32$$

Just like the beam shift update equation, the expectation is calculated over a range of α_k and β_k, and the combination of α_k and β_k that maximizes the expectation of the scene shift is chosen.

25

3.1.7 EM Algorithm Step 7

Repeat steps 5 and 6, replacing old estimates with newly found estimates. Each of the three update equations, Equation 24, Equation 28, and Equation 32 are dealt with iteratively. They each contain old estimates of parameters that are updated with every iteration of the algorithm. Once the new object is solved for, it is fed into the beam and scene update equations to gain shift estimates. Once these new estimates have been found, they are fed into the object update equation, and so on. This pattern of solving for new estimates of the object and shift parameters using the old estimates continues until the algorithm converges.

3.2 Testing Methods

Simulation

Algorithm testing began with experimentation in simulation. As shown in Step 1 of the algorithm derivation, the simulated incomplete data was created by convolving a simulated beam limited object with a PSF that simulates the atmospheric PSF.

The simulated target object is an image of a bar chart with width and height of 256 pixels. The original image is shown below in Figure 10.
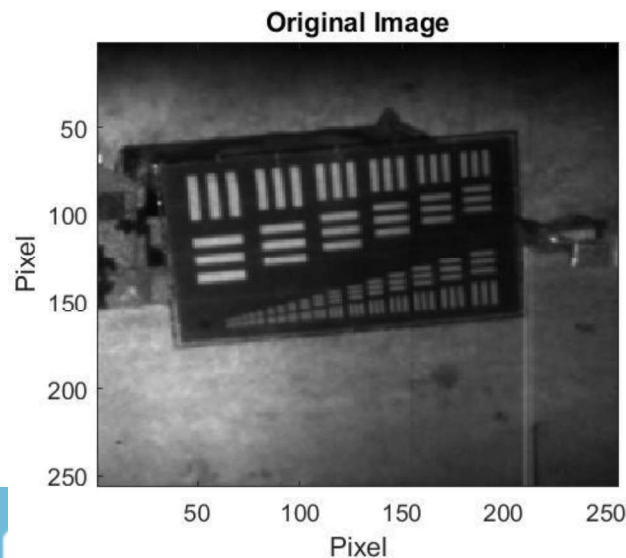

Figure 10: Original Image for Testing in Simulation

The simulated beam was given a two-dimensional Gaussian intensity profile with a standard deviation of 15 pixels. The beam was normalized, so the intensity at the center point is one. The beam is shown, below, in Figure 11 next to the beam limited FOV of the original image.
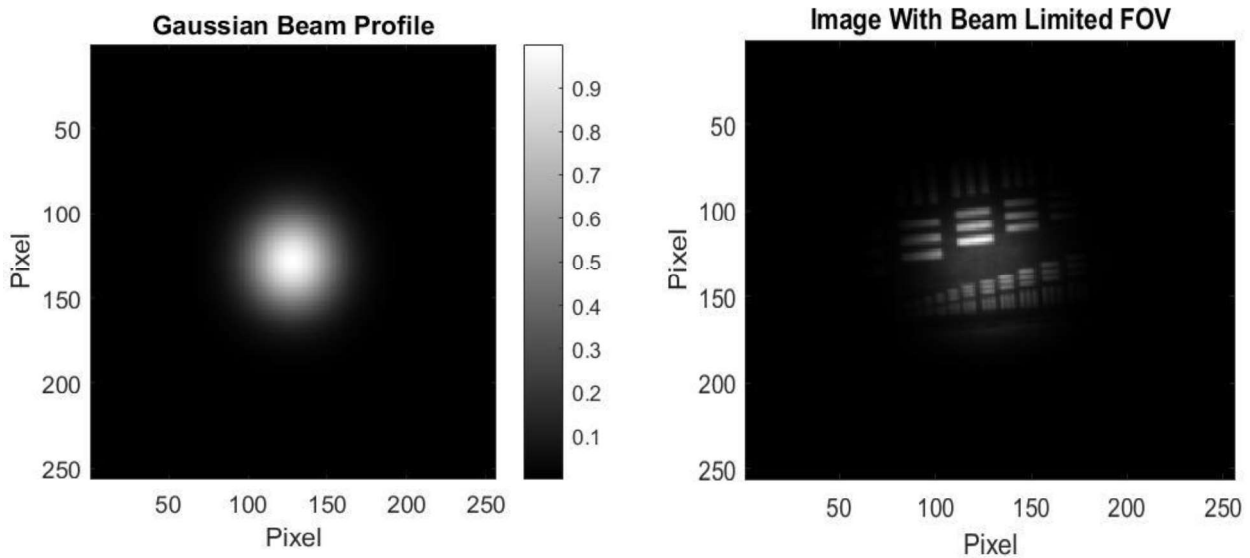

Figure 11: Beam Shape and Beam Limited FOV Object

The PSF was simulated by taking the autocorrelation of the pupil function, and then normalizing. With the PSF created, Equation 6 can be used to generate one frame of incomplete data by a convolution of the PSF with the beam limited image. This incomplete data, without any shifts or noise considerations, is shown in Figure 12.
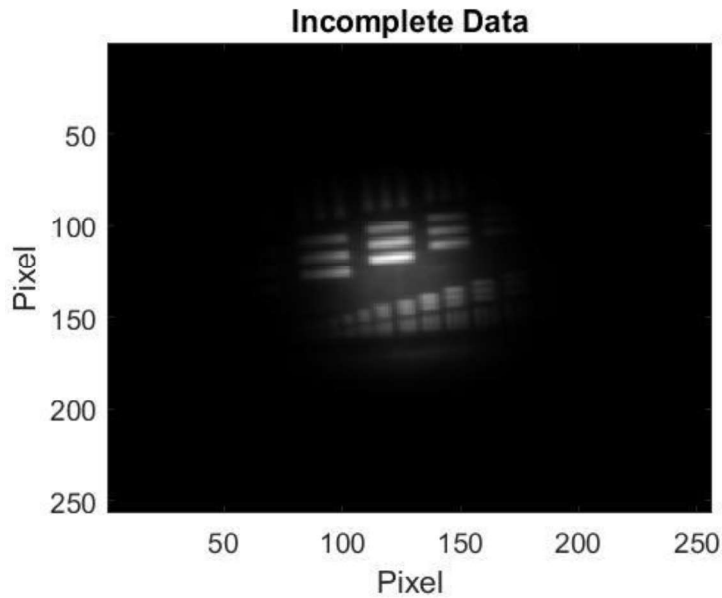
27

Figure 12: Incomplete Data with No Shifts or Noise Considerations

To finally complete the data set, noise considerations must be added to the incomplete data. Several noise sources must be considered: background noise, laser speckle, and photon counting noise. Testing was conducted using incomplete data without any noise added to see how the algorithm functions without any noise. Testing was also conducted with Poisson noise added; this simulates imaging an object with photon counting noise. Finally, testing was conducted with background noise and laser

28

speckle added. The background noise was simulated by generating Poisson random numbers with a mean of 50 photons to add to the image. The laser speckle noise is added in simulation with the gamma distribution. As discussed in Chapter 2, the laser speckle relies on a coherency factor that simulates the level of coherency of the illuminating light source. This research effort uses a coherency factor of 10 for the laser speckle simulation. Figure 13 shows samples of incomplete data with Poisson noise and speckle noise.
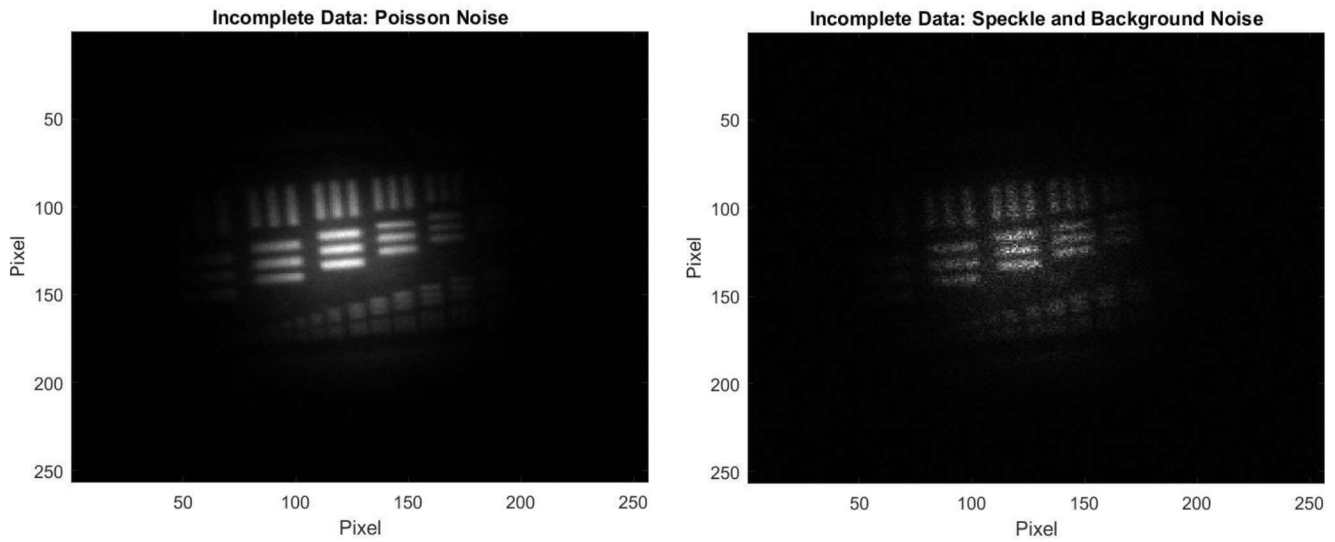

Figure 13: Incomplete Data with Poisson Noise and Speckle Noise

<center>**IV. Analysis and Results**</center>

This section provides results gathered in the simulation testing described earlier in Chapter III and discusses its performance compared to a cross-correlation method.

4.1 Simulated Data Results

This research effort began by testing each component of the algorithm independently. Once verifying that each component functions properly, each component was combined to form the EM algorithm. The EM algorithm was then tested and compared against the cross-correlation method. This section concludes by testing a hybrid algorithm which combines aspects of the EM algorithm and cross-correlation.

4.1.1 Isolated Component Testing

Simulated data testing began by testing each algorithm component individually. As discussed in the derivation in Chapter 3, The EM algorithm is composed of three components: beam shift update equation, scene shift update equation, and object optimization equation. To isolate each component, the truth data was given to algorithm for two components and the algorithm was left to estimate the final component individually. Once each component functions independently, they can be implemented together to formulate the complete EM algorithm.

4.1.1.1 Beam Shift Tracking

The beam shift update equation, Equation 28 shown again below, was tested first.

<center>30</center>

$$Q_b(\gamma_k, \varepsilon_k) =$$

$$\sum_k^K \sum_x^N \sum_y^N \sum_z^N \sum_w^N \frac{o^{old}b(z - \gamma_k^{old}, w - \varepsilon_k^{old})h(x - z - a_k^{old}, y - w - \beta_k^{old})d_k(x,y)}{\sum_z^N \sum_w^N o^{old}b(z - \gamma_k^{old}, w - \varepsilon_k^{old})h(x - z - a_k^{old}, y - w - \beta_k^{old})} \ln(b(z - \gamma_k, w - \varepsilon_k))$$

$$- \sum_k^K \sum_z^N \sum_w^N o(z,w)b(z - \gamma_k, w - \varepsilon_k)$$

A set of 1000 samples of incomplete data was created with randomly generated shifts in the beam and scene in x and y directions for each sample. The shift parameters were chosen to be a zero mean Gaussian random number with a standard deviation of 2 pixels. Each sample of incomplete data, $d_k(x, y)$, was fed into the beam shift update equation with the true object, $o(z, w)$, and the true scene shifts, α_k and β_k. The equation then estimates the beam shifts, γ_k and ε_k, present in each samples of incomplete data. Figure 14, below, shows the error in beam shift estimates from a set of incomplete data created without any noise considerations.
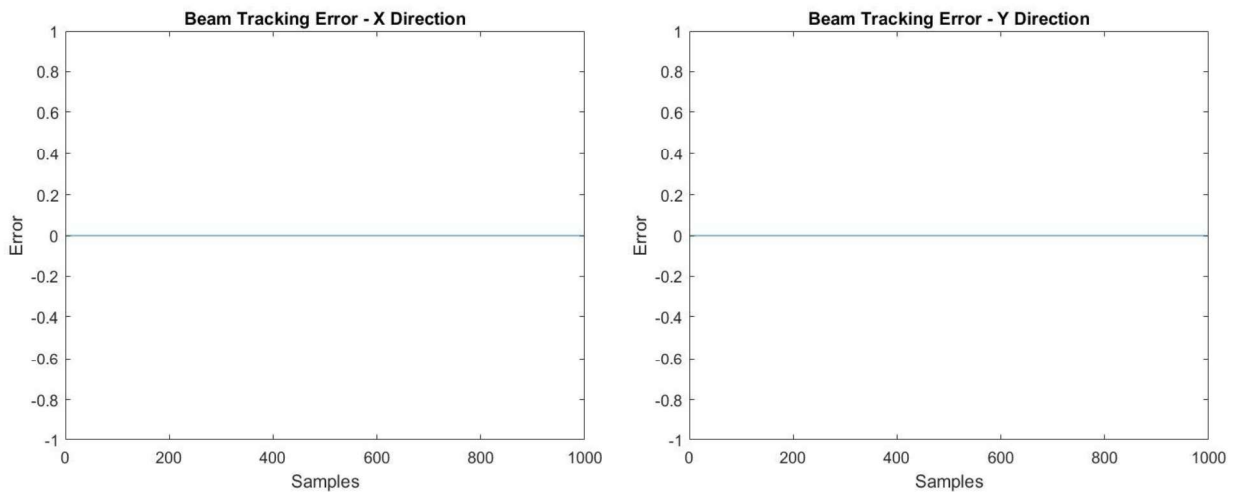

Figure 14: Beam Shift Tracking with No Noise

In a noiseless system, the beam update equation perfectly estimated the input beam shifts over 1000 trials - 0.0 shift error in both X and Y directions. This process was then repeated with Poisson noise added to the incomplete data in simulation. The results of this testing are shown below in Figure 16.
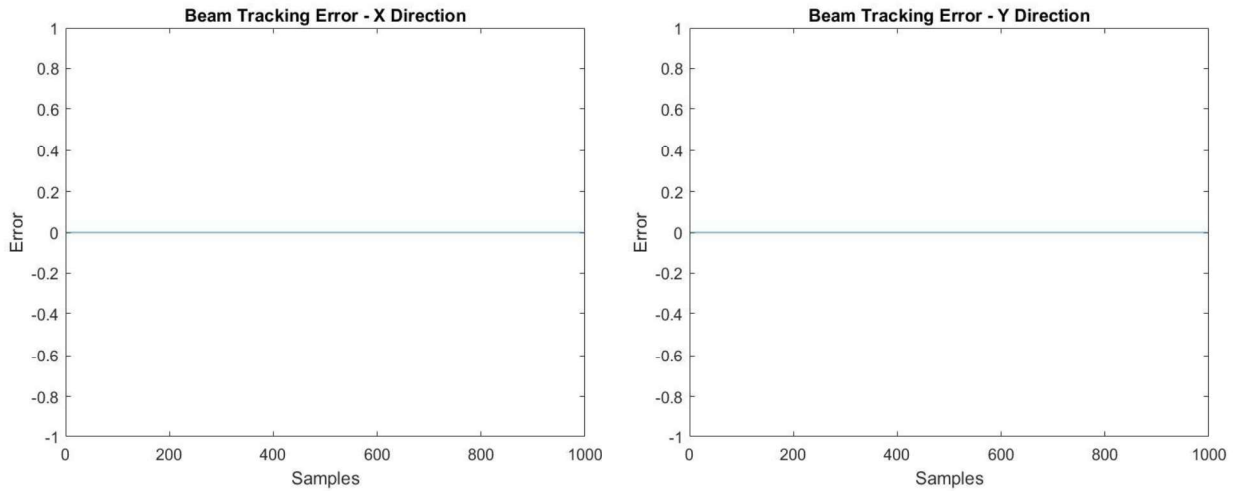

Figure 16: Beam Shift Tracking with Poisson Noise

The Poisson noise simulation also showed perfect beam tracking over 1000 trials. This process was finally repeated with speckle and background noise considerations added to the simulation. Results of this testing are shown below in Figure 15.
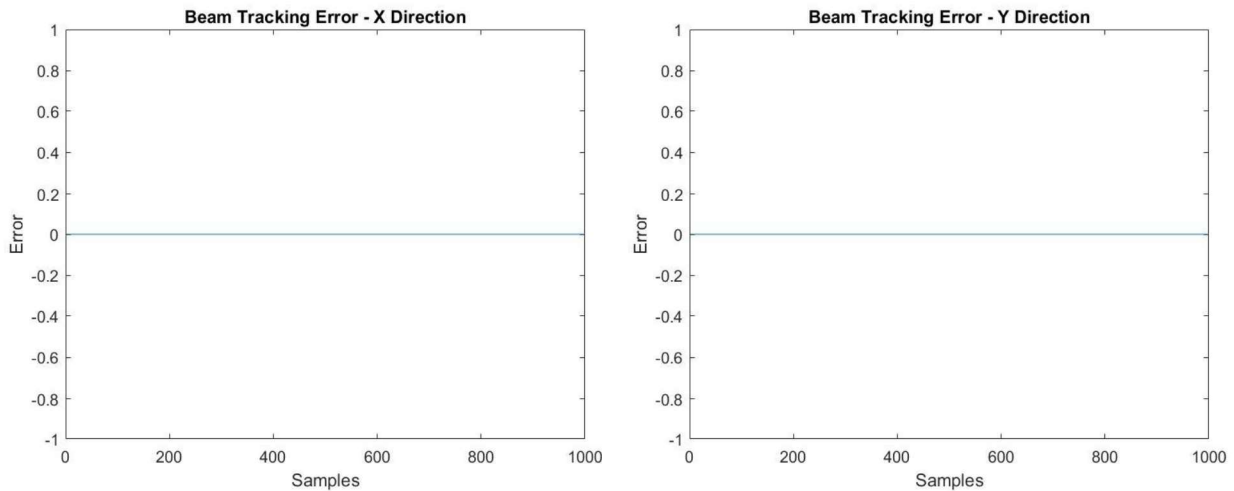

Figure 15: Beam Shift Tracking with Speckle Noise

The beam shift update equation again showed perfect ability to track input beam shifts with background and laser speckle noise considerations added to the simulation.

Each of these tests have demonstrated that the beam shift update equation can function properly when given true data for scene shifts and target object. Under each noise condition, the beam shift update equation perfectly estimated the input beam shifts. The research effort next moved to isolated testing of the scene tracking update equation.

4.1.1.2 Scene Shift Tracking

The scene update equation, Equation **32** shown again below, was tested next.

$$Q_S(\alpha_k, \beta_k) = \tag{32}$$

$$\sum_k^K \sum_x^N \sum_y^N \sum_z^N \sum_w^N \frac{o^{old} b\left(z - \gamma_k^{old}, w - \varepsilon_k^{old}\right) h\left(x - z - a_k^{old}, y - w - \beta_k^{old}\right) d_k(x,y)}{\sum_z^N \sum_w^N o^{old} b\left(z - \gamma_k^{old}, w - \varepsilon_k^{old}\right) h\left(x - z - a_k^{old}, y - w - \beta_k^{old}\right)} \, ln\left(h(x - z - \alpha_k, y - w - \beta_k)\right)$$

The true object and true beam shifts were fed into the simulation. This left the scene update equation to estimate only the α_k and β_k for each sample of incomplete data. The equation was tested again with a set of 1000 samples of incomplete data with randomly generated beam and scene shifts. The shift parameters were again chosen to be a zero mean Gaussian random number with a standard deviation of 2 pixels. Figure 17, below, shows the input and output shifts of a set of incomplete data created without any noise considerations.
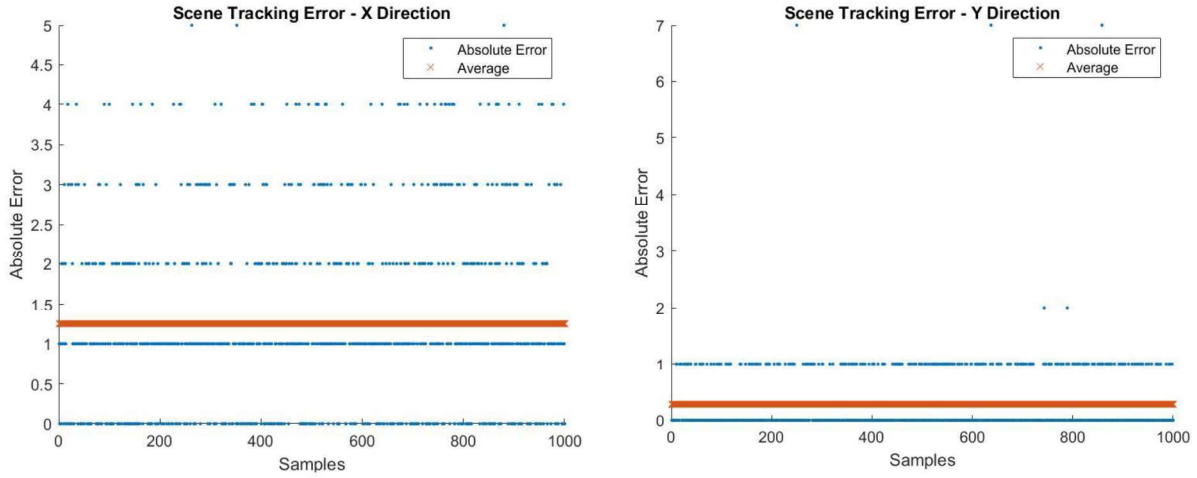
Figure 17: Scene Shift Tracking with No Noise

Given the true object and true beam shifts, the scene shift update equation was able to estimate the input shift with some success, but not perfectly. The mean absolute error in the x direction was 1.25 pixels and 0.29 pixels in the y direction. The mean absolute error was calculated according to Equation 33 , below. k is the frame of the incomplete data, K is the total number of samples, S_k^{est} is the estimated shift parameter, and S_k^{input} is the true input shift parameter.

$$E_{abs} = \frac{1}{K} \sum_{k}^{K} \left| S_k^{est} - S_k^{input} \right|$$

33

Next, testing continued with Poisson noise added to the simulation. The result of this testing is shown below in Figure 18.
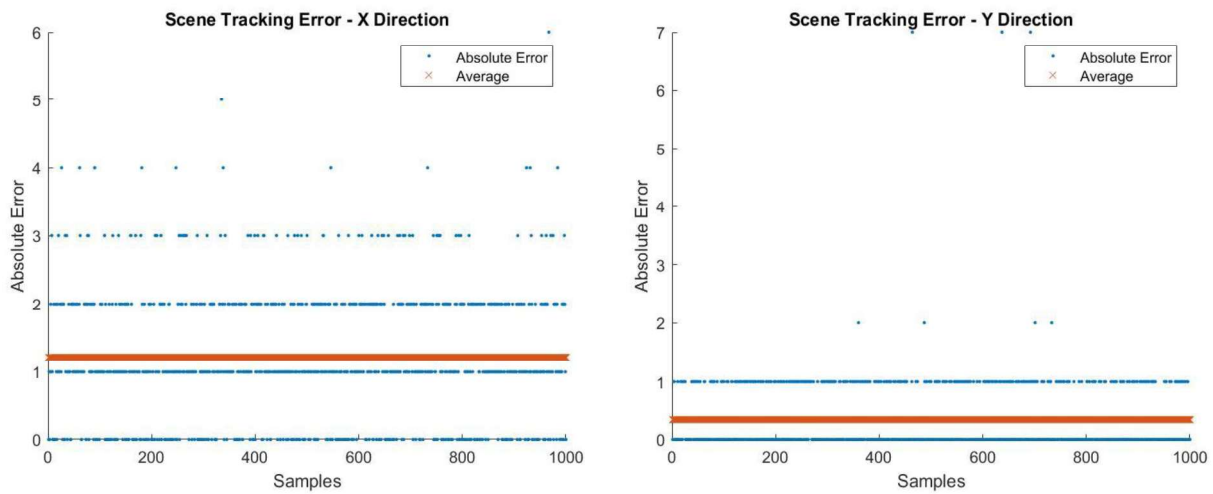
34

Figure 18: Scene Shift Tracking with Poisson Noise

The scene shift update equation was again able to estimate the input shift with some success, but not perfectly. The mean absolute error in the x direction was 1.21 pixels and 0.34 pixels in the y direction. Testing was repeated one final time with speckle noise and background noise added to the simulation. Results are shown below in Figure 19.
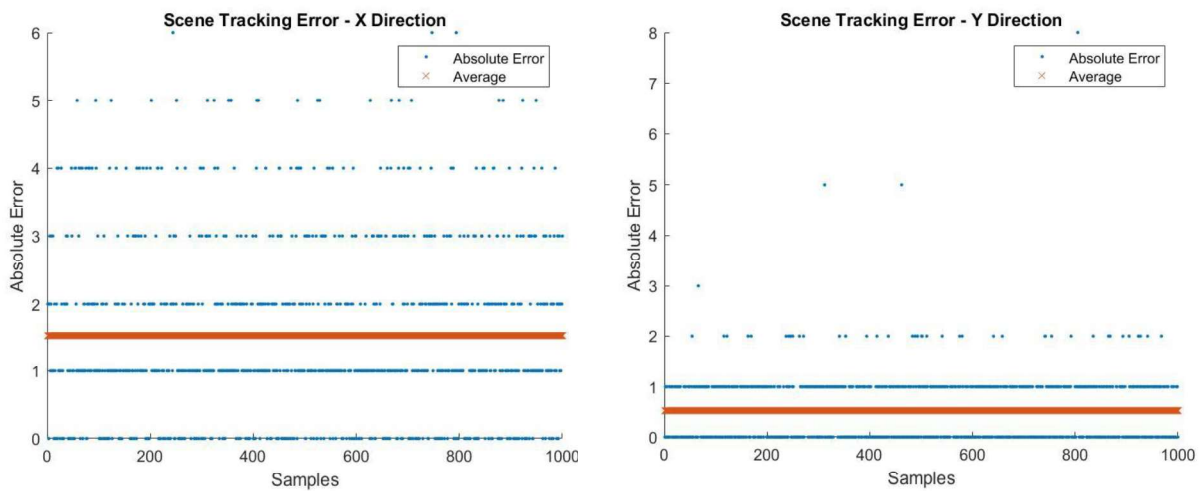

Figure 19: Scene Shift Tracking with Speckle Noise

35

When dealing with speckle and background noise added to the simulation, the scene shift update equation was again able to estimate the input shift with noticeably less accuracy than the Poisson or noiseless simulations. The mean absolute error in the x direction was 1.53 pixels and 0.54 pixels in the y direction.

Unlike the beam shift update equation, the scene shift update equation was not able to perfectly track the input shift. Given the true object and true beam shifts, the update equation showed some ability to track the shifting scene but failed to consistently estimate the input shift. Table 1, below, shows the absolute error in X and Y direction under each noise condition.

Table 1: Scene Shift Tracking Error

Noise Condition	X Absolute Error (pixels)	Y Absolute Error (pixels)
No Noise	1.25	0.29
Poisson Noise	1.21	0.34
Speckle Noise	1.53	0.54

Table 1 shows that the update equation performed comparably under no noise and Poisson noise, and it performed slightly worse with speckle noise added to the system. These results also show that the Y direction is clearly tracked better than the X direction - this is most likely due to prominent features in the original target image. The large

horizontal bars in the original image must make the equation estimate the Y direction shifts more easily than the X direction shifts.

The equation is likely unable to perfectly estimate the shifts due to computer limitations in the numerical calculations. The derivation of this scene shift update equation from the EM algorithm should converge on the correct input shifts, but these results show that in simulation the update equation does not converge on the true shift.

4.1.1.3 Object Optimization

The last update equation tested was the object optimization update equation, shown below in Equation 24.

$$o(z_0, w_o) = \qquad\qquad 24$$

$$\frac{\sum_k^K \sum_x^N \sum_y^N \frac{o^{old} b\left(z - \gamma_k{}^{old}, w - \varepsilon_k{}^{old}\right) h\left(x - z - \alpha_k{}^{old}, y - w - \beta_k{}^{old}\right) d_k(x,y)}{\sum_z^N \sum_w^N o^{old} b\left(z - \gamma_k^{old}, w - \varepsilon_k^{old}\right) h\left(x - z - a_k^{old}, y - w - \beta_k^{old}\right)}}{\sum_k^K b(z_0 - \gamma_k, w_o - \varepsilon_k)}$$

Similar to the beam and scene equation testing, the equation was tested again with a set of thirty samples of incomplete data with randomly generated beam and scene shifts. The shift parameters were again chosen to be a zero mean Gaussian random number with a standard deviation of 2 pixels. The true beam and scene shifts were then fed into the simulation. This left the object update equation to estimate only the object, $o(z, w)$. Figure 20, below, shows one frame of the incomplete data input and the optimized object using the set of incomplete data created without any noise considerations.
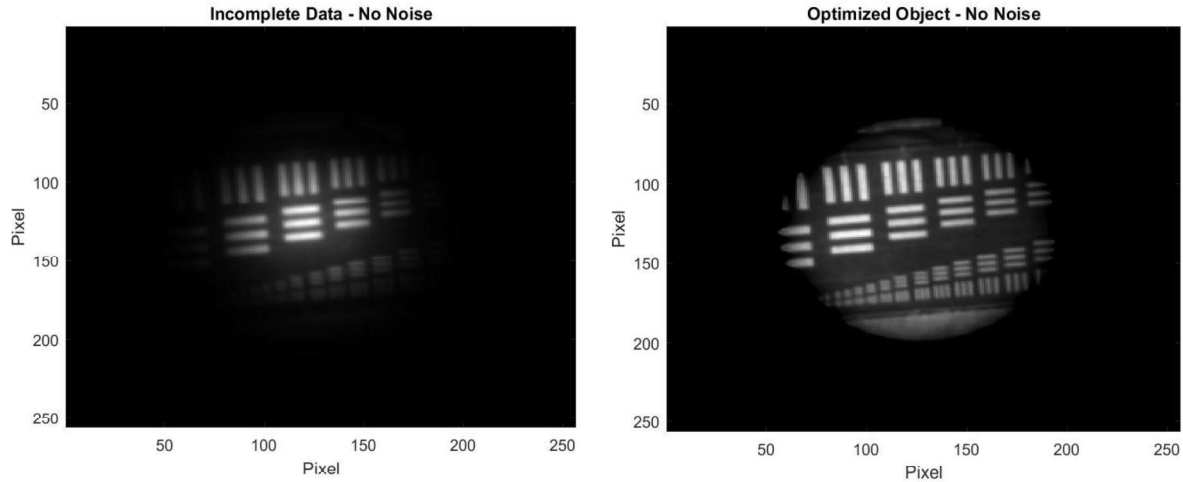
Figure 20: Incomplete Data and Optimized Object with No Noise

Simple visual analysis shows that the optimized object produces a noticeably cleaner image. The details of each of the bars in the bar chart are much sharper in optimized object than the incomplete data. The deconvolution component in the EM algorithm also widens the FOV of the target. The algorithm accounts for the beam shape and widens the FOV of the object. This gives much more information about the true target object than the incomplete data, and provides a noticeably better representation of the target.

Beyond simple visual analysis, Root Mean Squared Error (RMSE) was used to analyze the results of the output images. RMSE was calculated according to Equation 34, below.

$$RMSE = \sqrt{\frac{\sum_{w}^{N}\sum_{z}^{N}(o_{est}(z,w) - o_{true}(z,w))^2}{N^2}} \qquad 34$$

The RMSE for the incomplete data is 156.17 compared to 15.73 for the optimized object. This drastic improvement in RMSE confirms the visual analysis that the object is optimized through this object optimization equation. This testing continued with Poisson noise added to the system. Figure 21, below, shows the results of object optimization in simulation under Poisson noise.
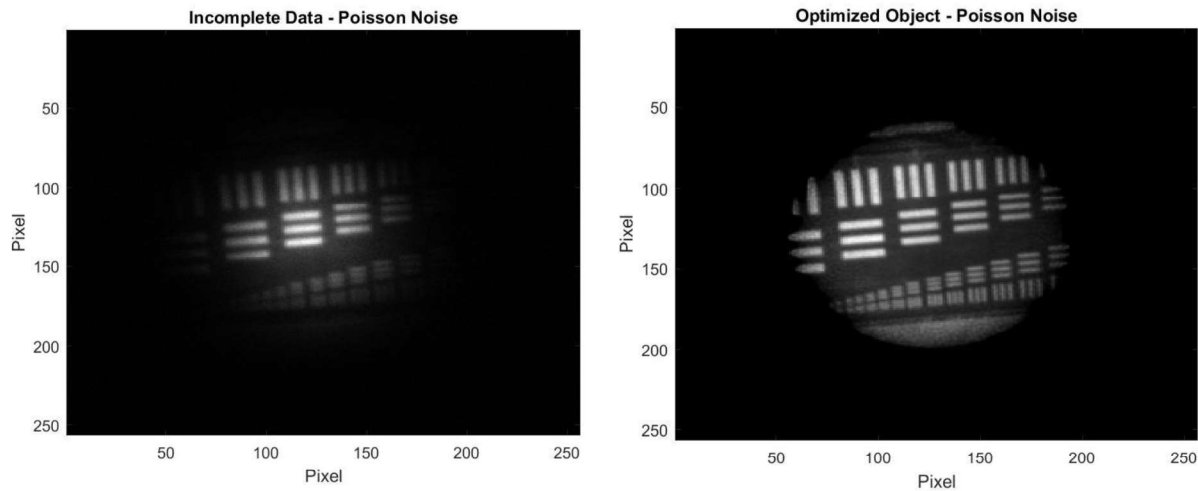

Figure 21: Incomplete Data and Optimized Object with Poisson Noise

Visual analysis again shows a vast improvement in clarity in the optimized image and again shows more information about the object with a wider field of view. RMSE analysis supports the visual analysis – RMSE was found to be 158.27 for the original incomplete data compared to 17.24 for the optimized image. This update equation was finally tested with speckle noise and background noise added to the simulation. These results are shown in Figure 22.
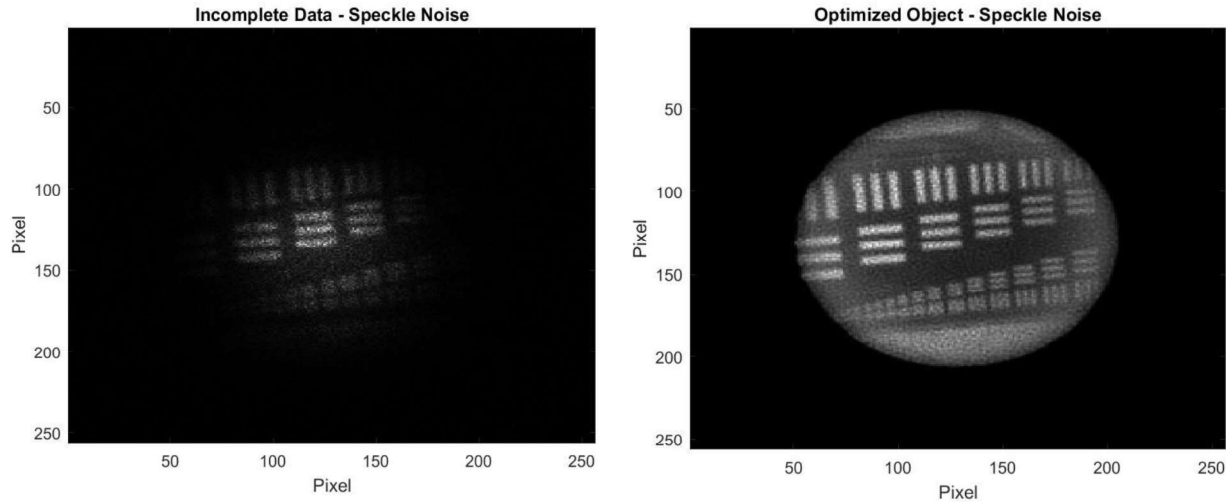
39

Figure 22: Incomplete Data and Optimized Object with Speckle Noise

The speckle noise simulation showed the biggest visual improvement in image clarity. The incomplete data, obscured with speckle noise, is almost indistinguishable. The optimized object shows a vastly improved image – the image still shows signs of noise, but the object is clearly visible in the output image. RMSE again supports the qualitative analysis that the object is significantly improved. The RMSE of the original incomplete data is 199.30 compared to 36.15 for the optimized object. Table 2 summarizes the results of each test under varying noise conditions. Testing the object update equation under each noise condition shows that it functions properly when given the true beam and scene input shifts.

Table 2: Summary of Object Testing Under Multiple Noise Conditions

Noise Condition	EM RMSE	Inc Data RMSE
No Noise	15.73	156.17
Poisson Noise	17.24	158.27
Speckle Noise	36.15	199.3

4.1.2 EM Algorithm

After confirming that each update equation worked properly individually, the whole EM beam and scene tracking deconvolution algorithm was built by incorporating each update equation together. A set of thirty samples of incomplete data with randomly generated beam and scene shifts was generated. The shift parameters were again chosen to be a zero mean Gaussian random number with a standard deviation of 2 pixels.

The three update equations were integrated as shown in Figure 23. The incomplete data was fed into the object update equation, first. As opposed to feeding the true beam shift and true scene shifts, the algorithm was initialized by feeding in a zero shifted beam and zero shifted OTF. After one iteration of the object update equation, this newly estimated object is fed into the scene shift update equation with the zero shifted beam. The newly acquired scene shifts are then fed into the beam shift update equation with the newly estimated object. Once the beam shifts are estimated, these newly estimated scene shifts and beam shifts are then fed back into the object update equation, and the process continues iteratively until each equation converges on a single estimate

41

for the shifts or object estimate. After convergence, further iterations through each
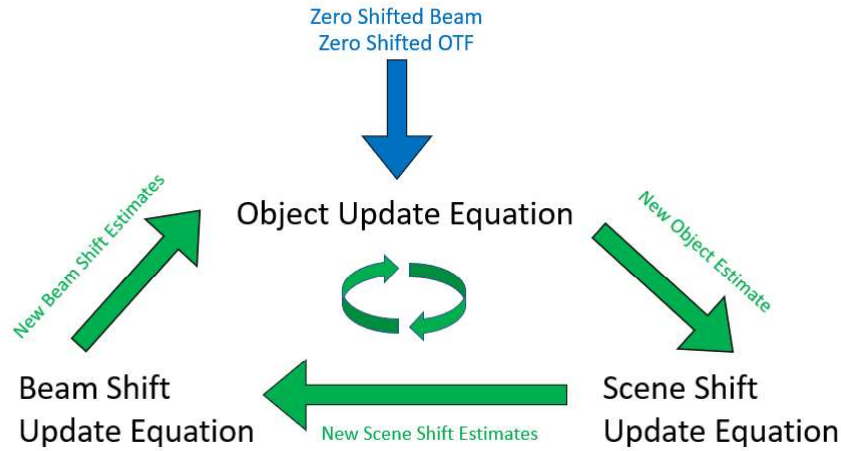component equation provide no improvement.

Figure 23: EM Algorithm Flow Chart

As discussed in Chapter 2, this research effort will compare results against cross-
correlation method. Cross-correlation will provide estimates for the scene shifts in the X
and Y directions but cannot estimate beam shifts. These estimated shifts can then be used
to align samples of incomplete data to provide an estimate of the object. This research
will compare estimates of scene shifts from the EM algorithm against estimates from the
cross-correlation method. The research will then compare the optimized object from the
EM algorithm and compare against the estimated object utilizing scene shift estimates
from the cross-correlation method.

4.1.2.1 Noiseless Simulation

Initial testing of the whole algorithm began again with noiseless data. The algorithm converged on beam shifts, scene shifts, and an optimized object, and the results of each are shown below.
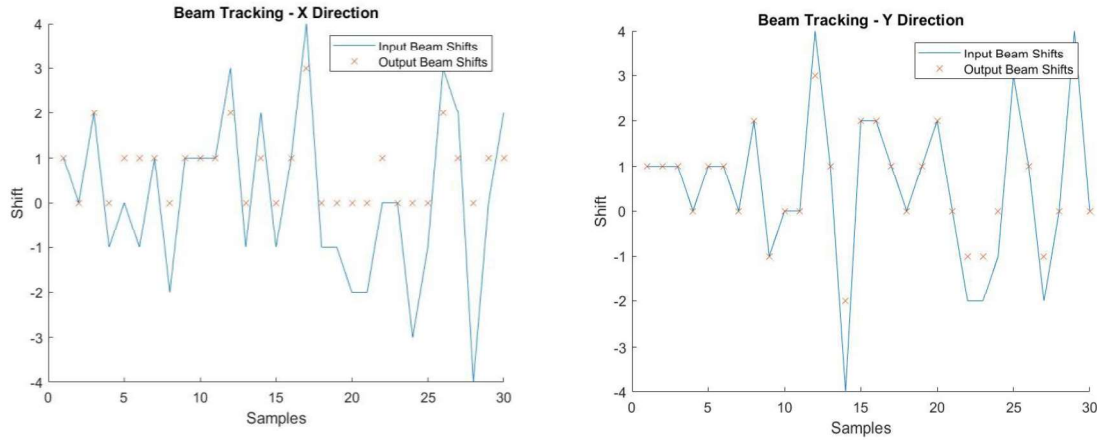

Figure 24: Beam Shift Tracking with No Noise

Figure 24, above, shows the shift tracking in the beam. Unlike the isolated beam update equation testing, the beam shifts were not perfectly tracked using the whole algorithm. The mean absolute error in beam shift tracking was 1.00 pixels in the X direction and 0.27 pixels in the Y direction. The results of the scene tracking are shown below in Figure 25.
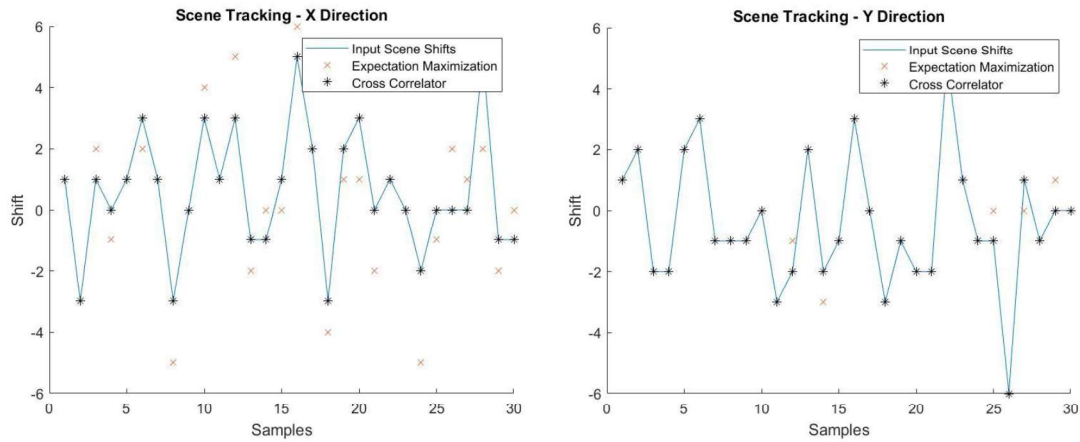
Figure 25: Scene Shift Tacking with No Noise

Figure 25 shows the shift tracking in the scene from the EM algorithm and the cross-correlation method. The cross-correlation method tracked the scene shifts perfectly in both X and Y directions - resulting in an absolute mean error of 0.0 pixels in each direction. The EM algorithm did not perfectly track the input shifts. The EM algorithm produces a mean absolute error of 1.07 pixels in the X direction and 0.17 pixels in the Y direction.
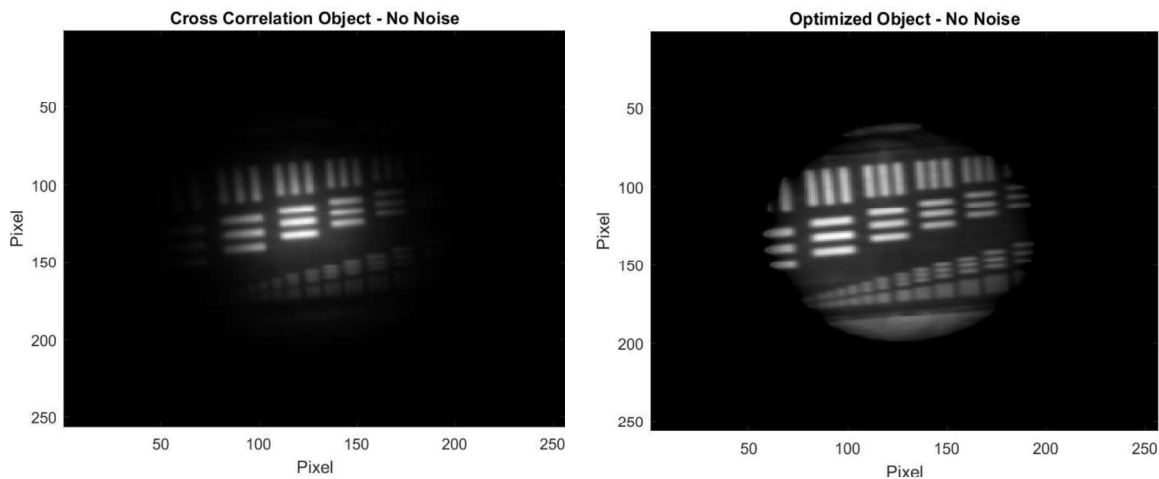
Figure 26: Cross-Correlation Object and EM Object with No Noise

Figure 26 shows the final optimized image of the EM algorithm compared against the output image from the cross-correlation method. Visual analysis of both images show that the EM algorithm greatly widens the field of view of the estimated object. The cross-correlation object shows sharp detail of the bars in the center of the bar chart, but the object is limited by the beam's FOV. The EM algorithm optimized object provides a much larger FOV giving more information about the target object. Because the scene shifts were not tracked perfectly, the details of the bars are not as sharp as the cross-correlation object. However, the EM object's wider FOV of the target object increases the information present in the image. The added information throughout the image decreases the error in the optimized object. The RMSE of the cross-correlation object was 155.81 compared to 45.10 for the optimized object.

4.1.2.2 Poisson Noise Simulation

Testing continued with Poisson noise added to the simulation, and the results were again compared against the cross-correlation method. The beam shift tracking results are shown, below, in Figure 27.
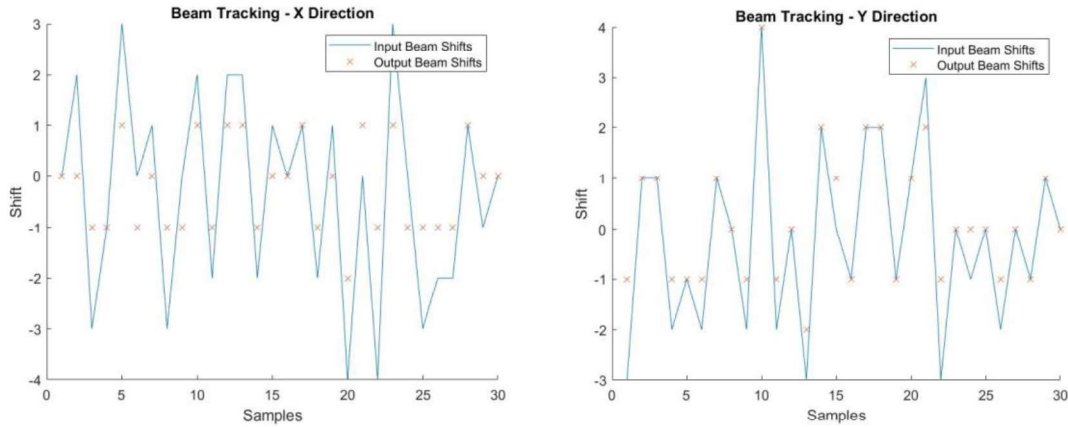

Figure 27: Beam Shift Tracking in X and Y Directions with Poisson Noise

Figure 27, above, shows the shift tracking in the beam. The beam shifts again tracked the beam effectively, but not perfectly, using the whole algorithm. The mean absolute error in beam shift tracking was 1.10 pixels in the X direction and 0.43 pixels in the Y direction. The results of the scene tracking are shown below in Figure 28.
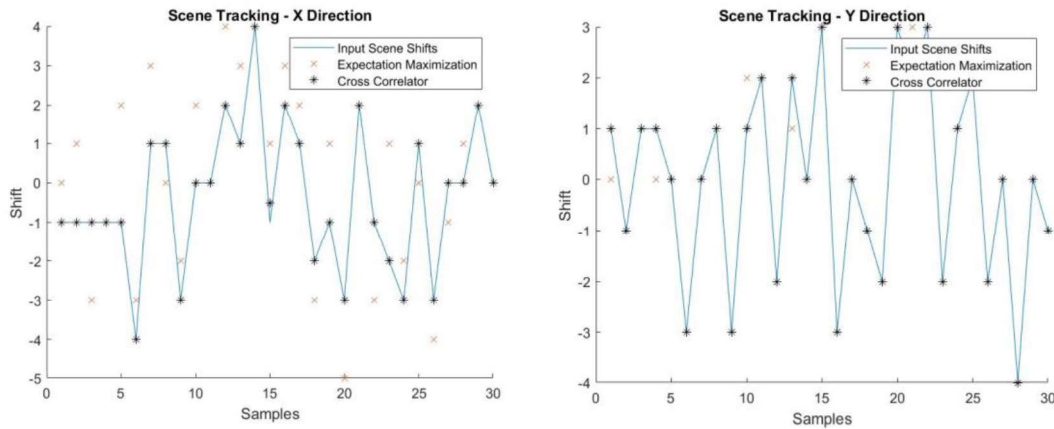
Figure 28: Scene Shift Tracking in X and Y Directions with Poisson Noise

Figure 28 shows the shift tracking in the scene from the EM algorithm and the cross-correlation method. The cross-correlation method tracked the scene shifts perfectly in both X and Y directions - resulting in an absolute mean error of 0.0 pixels in each direction. The EM algorithm did not perfectly track the input shifts. The EM algorithm produces a mean absolute error of 1.27 pixels in the X direction and 0.20 pixels in the Y direction.

Figure 29 shows the final optimized image of the EM algorithm compared against the output image from the cross-correlation method. Visual analysis again shows that the EM algorithm greatly widens the FOV of the estimated object. Similar to the noiseless simulation, the cross-correlation object shows sharp detail of the bars in the center of the bar chart, but the object is limited by the beam's FOV. The EM algorithm optimized object provides a much larger FOV giving more information about the target object. Just like the noiseless simulation, the scene shifts were not tracked perfectly, so the details of the bars are not as sharp as the cross-correlation object. However, the wider FOV again increases the overall amount of information present in the image. This decreases the error

47

in the EM object. The RMSE of the cross-correlation object was 155.90 compared to
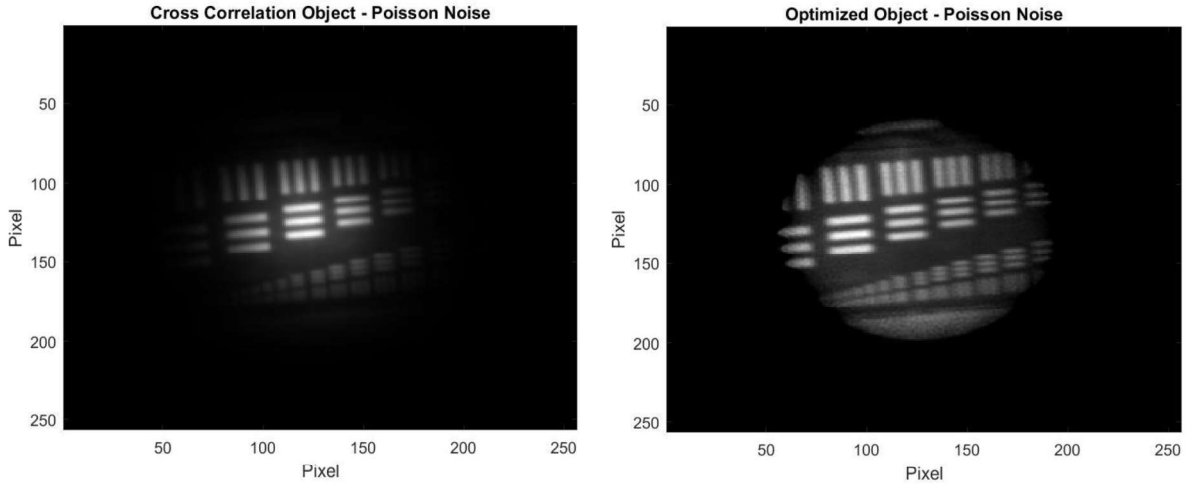
47.73 for the optimized object.

Figure 29: Cross-Correlation Object and EM Object with Poisson Noise

4.1.2.3 Laser Speckle and Background Noise Simulation

Testing concluded with background and laser speckle noise sources added to the

simulation. Results of the beam shift tracking are shown, below, in Figure 30.
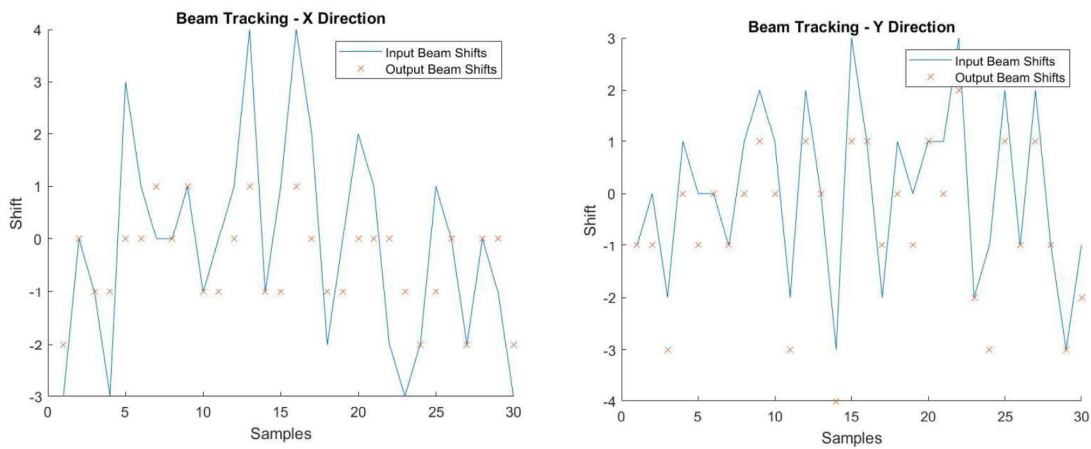

Figure 30: Beam Shift Tracking with Speckle Noise

48

The beam shifts were again tracked with some success but not perfectly. The mean absolute error in beam shift tracking was 1.10 pixels in the X direction and 0.73 pixels in the Y direction. Next, the results of the scene tracking are shown, below, in Figure 31.
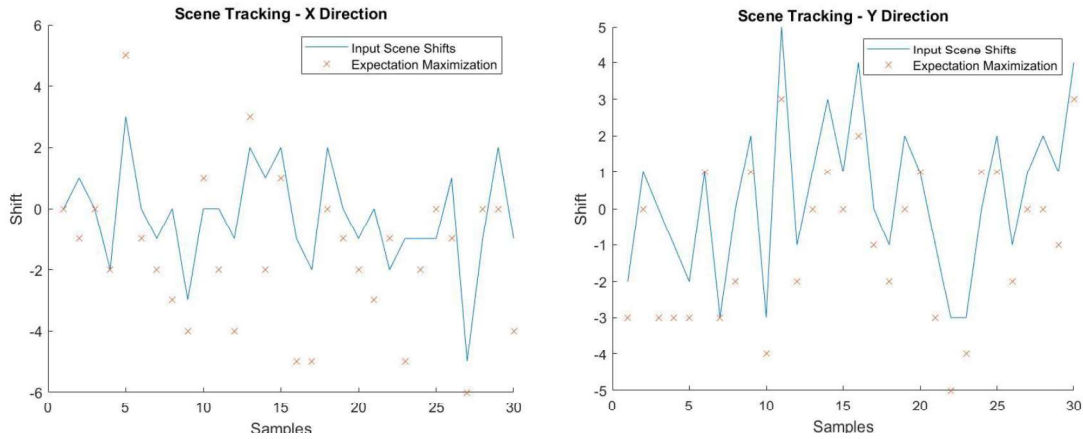

Figure 31: Scene Shift Tracking in X and Y Directions with Speckle Noise

With speckle and background noise added to the simulation, the cross-correlation method failed to track the scene shifts perfectly. The cross-correlation method gave an absolute mean error of 0.60 pixels in the X direction and 0.57 in the Y direction. The EM algorithm produced a mean absolute error of 1.20 pixels in the X direction and 0.23 pixels in the Y direction.

Figure 32 shows the final optimized image of the EM algorithm compared against the output image from the cross-correlation method. Visual analysis again shows that the EM algorithm greatly widens the FOV of the estimated object. The cross-correlation object is limited again by the FOV of the beam. Unlike the previous simulations, the cross-correlation object does not provide sharp detail of the bars, due to the noisy incomplete data. The EM optimized object provides a much larger FOV giving more

49

information about the target object. The wider FOV again increases the overall quality of the object image. Quantitative analysis again supports the visual analysis; the RMSE of the cross-correlation object was 151.17 compared to 65.24 for the optimized object.
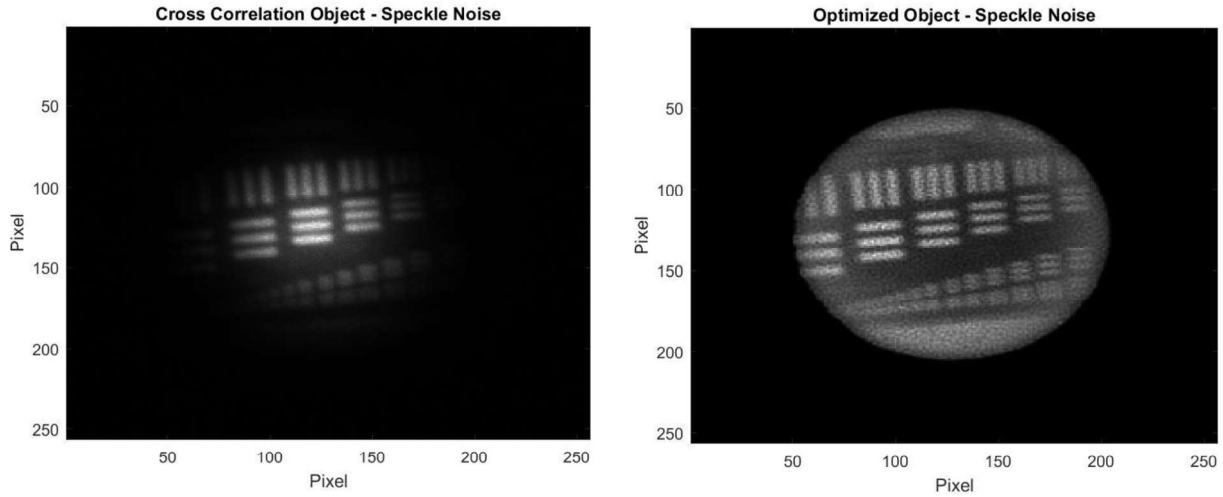

Figure 32: Cross-Correlation Object and EM Object with Speckle Noise

Table 3: EM Algorithm Summary of Results

Noise Condition	Beam Absolute Error - X (pixels)	Beam Absolute Error - Y (pixels)	Scene Absolute Error - X (pixels)	Scene Absolute Error - Y (pixels)	Cross-Corr Absolute Error - X (pixels)	Cross-Corr Absolute Error - Y (pixels)	EM RMSE	CC RMSE
No Noise	1.00	0.27	1.07	0.17	0.00	0.00	45.10	155.81
Poisson Noise	1.10	0.43	1.27	0.20	0.00	0.00	47.73	155.90
Speckle Noise	1.10	0.73	1.20	0.23	0.60	0.57	65.24	151.17

50

4.1.3 Hybrid Algorithm

After comparing the EM algorithm against the cross-correlation method, the EM algorithm clearly produces a cleaner output image than the cross-correlation method. The previous data also shows that the cross-correlation method tracks the scene shifts better than the EM algorithm due to computational limitations. Testing continued to see if a hybrid method could produce better results using cross-correlation shifts with the EM beam shift update equation and EM object update equation. The process flow for the hybrid algorithm is shown, below, in Figure 33.
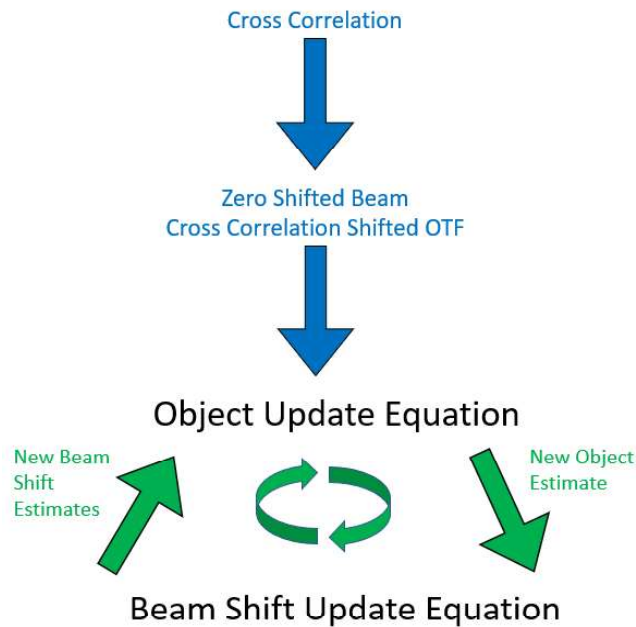

Figure 33: Hybrid Algorithm Flow Chart

The cross-correlation algorithm estimates the scene shifts in each frame of the data set. These estimated shifts are then fed into the object update equation. The new estimate of the object is then given to the beam shift update equation with the cross-

correlation scene estimates. Next, the new beam shift estimates are given back to the object update equation. This process repeats until beam shift estimates and the object converge.

4.1.3.1 Noiseless Simulation

This hybrid method was first tested using noiseless data. The beam tracking estimates are shown in Figure 34.
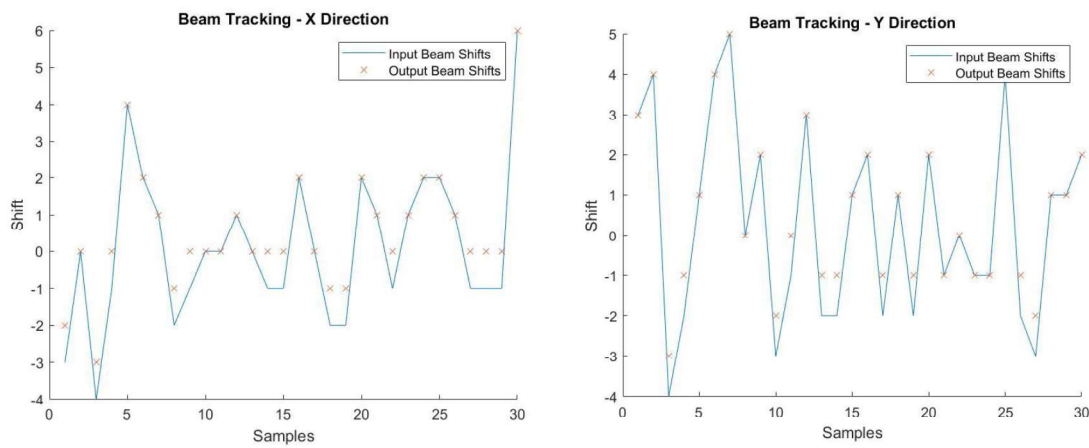

Figure 34: Beam Shift Tracking with No Noise

The beam shifts estimates show a marked improvement from the EM algorithm, but still do not track input shifts perfectly. The mean absolute error in beam shift tracking was 0.43 pixels in the X direction and 0.33 pixels in the Y direction. Next, the results of the cross-correlation shift tracking are shown, below, in Figure 35.

52

Figure 35: Scene Shift Tracking with No Noise

The cross-correlation method tracked the scene shifts perfectly in both X and Y directions - resulting in an absolute mean error of 0.0 pixels in each direction. Using these cross-correlation estimates and the EM algorithm beam shift estimates, the hybrid algorithm produced the object shown in Figure 36.

Figure 36: Hybrid Optimized Object with No Noise

This hybrid approach produced a strikingly clear image of the optimized object. The bars in the object are shown in sharp detail, and the FOV of the target is widened just like the EM optimized object before. This results in a RMSE of 16.89. This low RMSE for the hybrid image supports the visual assessment of a strikingly clear image.

4.1.3.2 Poisson Noise Simulation

The hybrid method was next tested using a data set with simulated Poisson noise added. The beam tracking estimates are shown in Figure 37.
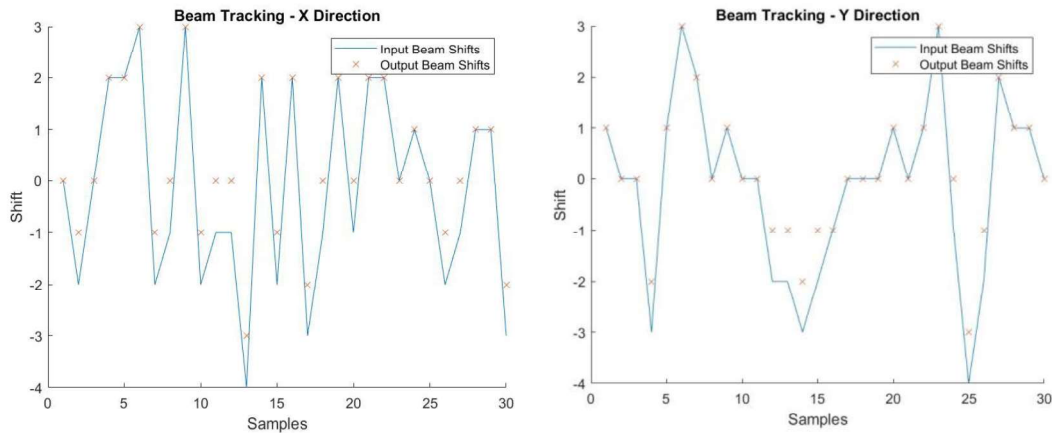
Figure 37: Beam Shift Tracking with Poisson Noise

The beam shift estimates, again, show a marked improvement from the EM algorithm, but still do not track input shifts perfectly. The mean absolute error in beam shift tracking was 0.47 pixels in the X direction and 0.27 pixels in the Y direction. Next, the results of the cross-correlation shift tracking are shown, below, in Figure 39.
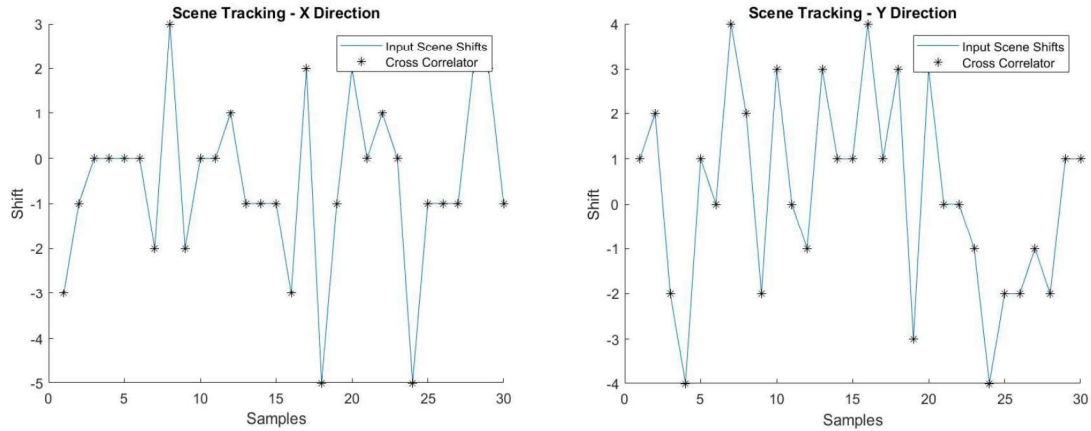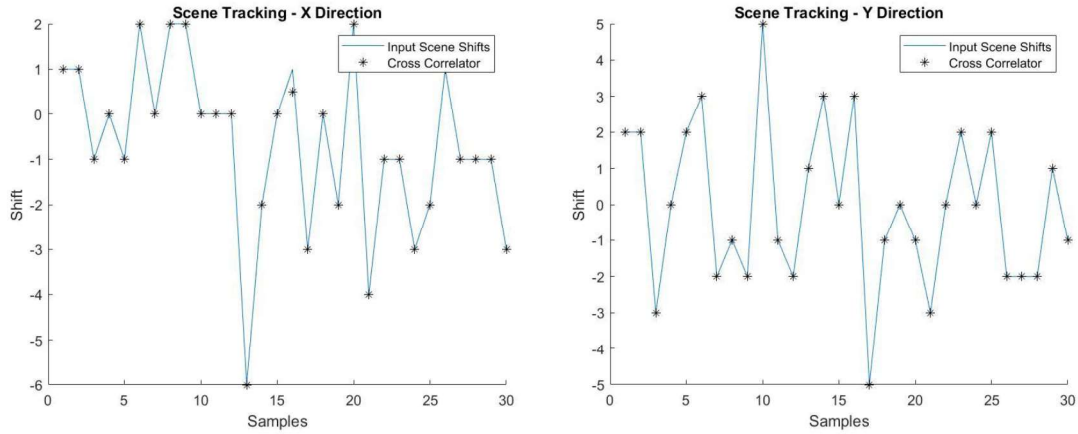
Figure 39: Scene Shift Tracking with Poisson Noise

The cross-correlation method tracked the scene shifts perfectly in both X and Y directions - resulting in an absolute mean error of 0.0 pixels in each direction. Using these cross-correlation estimates and the EM algorithm beam shift estimates, the hybrid algorithm produced the object shown in Figure 38.
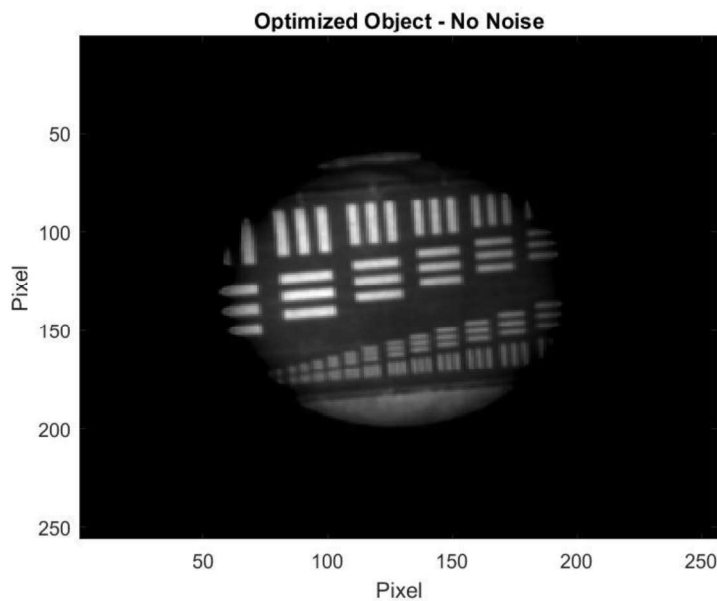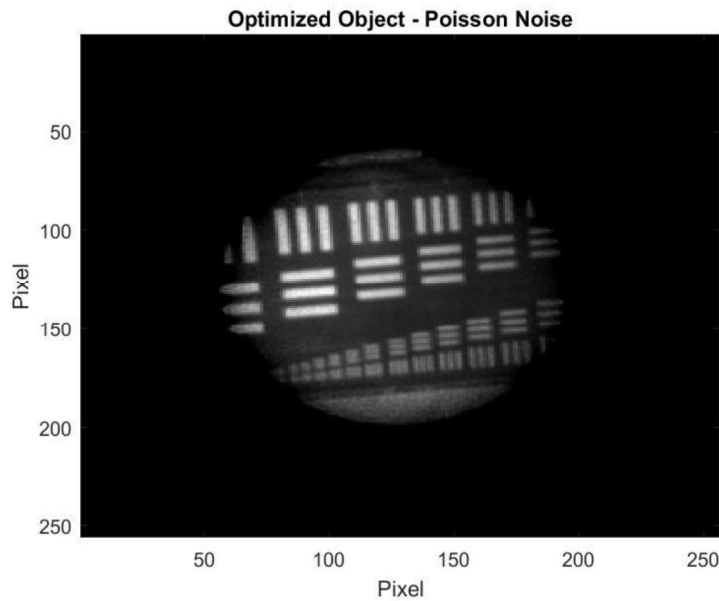

Figure 38: Hybrid Optimized Object with Poisson Noise

Even with Poisson noise added to the simulation, the hybrid approach produced another clean image of the optimized object. The bars in the object are again shown in sharp detail, and the FOV of the target is widened just like the EM optimized object before. Looking closely, there is some evidence of noise in the image towards the fringes of the object. However, the object is effectively optimized to show a clear object. This results in a RMSE of 21.77 for this image. This low RMSE for the hybrid image supports the visual assessment of another cleanly optimized image.

4.1.3.2 Laser Speckle and Background Noise Simulation

Finally, the hybrid method was tested using a data set with simulated laser speckle noise and background noise added. The beam tracking estimates are shown in Figure 40.
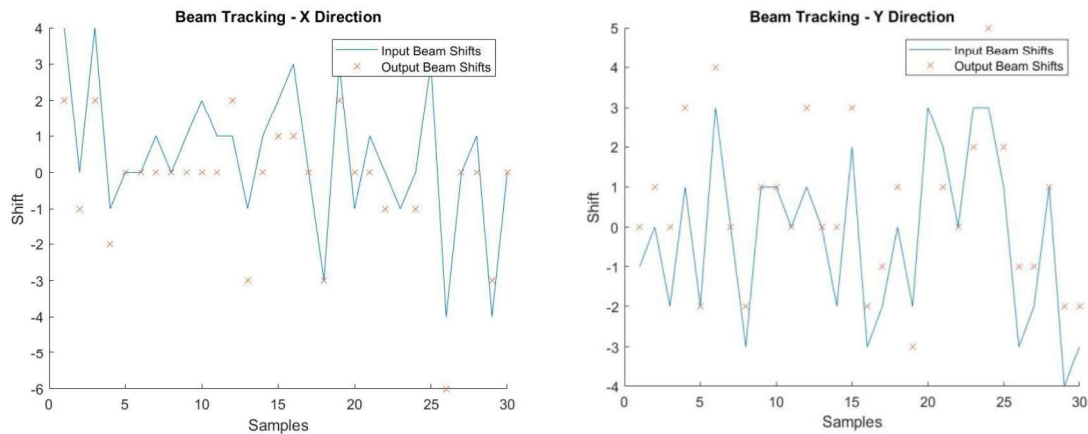
Figure 40: Beam Shift Tracking with Speckle Noise

The hybrid approach beam shift estimates show comparable results to the EM algorithm. The mean absolute error in beam shift tracking was 1.03 pixels in the X direction and 0.97 pixels in the Y direction. Next, the results of the cross-correlation shift tracking are shown, below, in Figure 41.
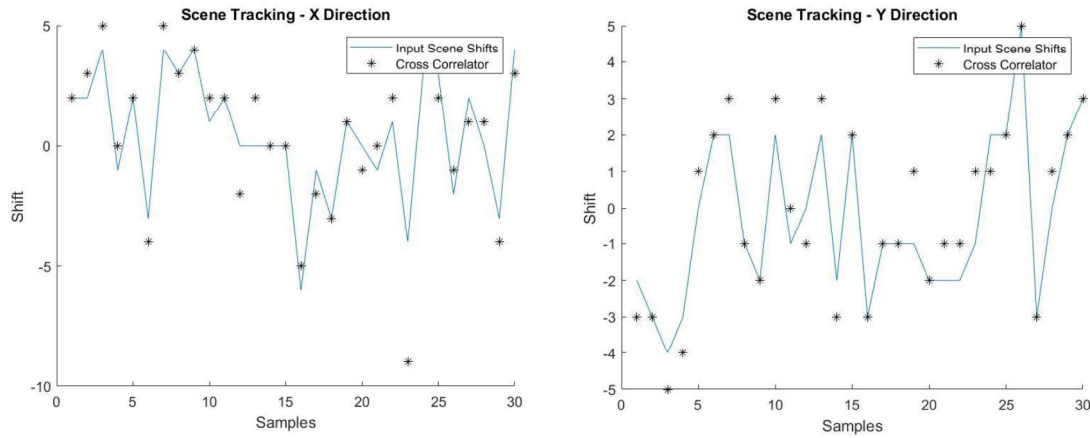

Figure 41: Scene Shift Tracking with Speckle Noise

Like the cross-correlation scene tracking results in the speckle noise simulation prior, the cross-correlation method tracked the scene shifts effectively, but not perfectly. This resulted in an absolute mean error of 0.90 pixels in the X direction and 0.60 pixels in the Y direction. Using these cross-correlation estimates and the EM algorithm beam shift estimates, the hybrid algorithm produced the object shown in Figure 42.

57
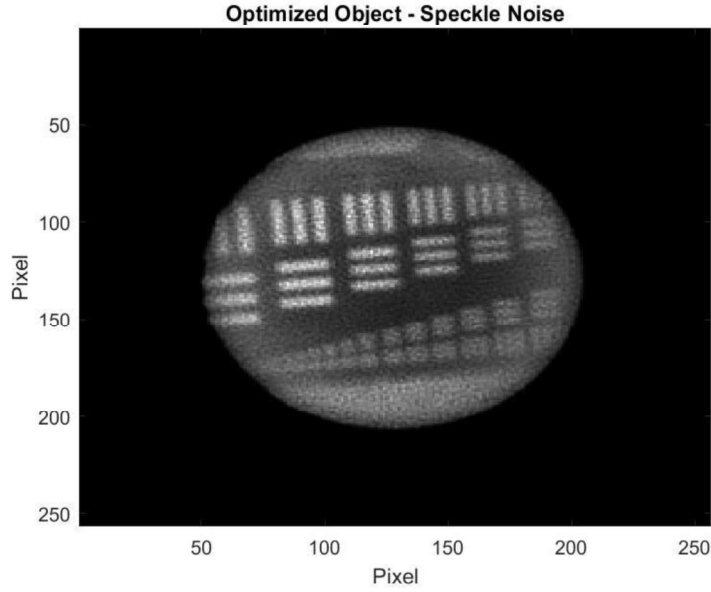
Figure 42: Hybrid Optimized Object with Speckle Noise

Because the scene and beam shift estimates are comparable to the EM algorithm, the hybrid approach, predictably, produced an output object comparable to the EM algorithm. The hybrid optimized object provides a large FOV, but the details are not as crisp as the previous hybrid results. There is clear noise throughout the image. However, the object is effectively optimized to show a clear object. This results in a RMSE of 61.92 for this image.

58

Table 4: Hybrid Algorithm Summary of Results

Noise Condition	Beam Absolute Error - X (pixels)	Beam Absolute Error - Y (pixels)	Cross-Corr Absolute Error - X (pixels)	Cross-Corr Absolute Error - Y (pixels)	Hybrid RMSE
No Noise	0.43	0.33	0.00	0.00	16.89
Poisson Noise	0.47	0.27	0.00	0.00	21.77
Speckle Noise	1.03	0.97	0.90	0.60	61.92

4.2 Analysis of Results

This thesis will first analyze the results of the EM algorithm before analyzing the hybrid method and the wholistic results of the research effort.

4.2.1 EM Algorithm Analysis

Though the beam could not perfectly track the input shift, it did track beam shifting with some success. Beam tracking results are shown in Figure 43, below. When isolated with the true object and scene shifts, the beam update equation individually tracked the input shifts perfectly. Without the true scene shifts and object, it was unable to perfectly estimate the input shifts, but it did provide close estimates. Looking at each noise source, the beam shift tracking, as expected, performed best under no noise condition with 1.00 pixels and 0.27 pixels of absolute error in X and Y, respectively. Once Poisson noise was added, it performed worse - but not much worse. The absolute

59

error in X only grew to 1.10 pixels, and the absolute error in Y only grew to 0.43 pixels. These are certainly less accurate than the noiseless simulation, but not drastically worse. Once laser speckle noise and background noise sources were added, the performance decreased, but only slightly. The absolute error in X remained steady at 1.10 pixels, and the absolute error in Y only grew to 0.73 pixels. These results suggest that the beam tracking can handle various noise sources successfully, though not perfectly.
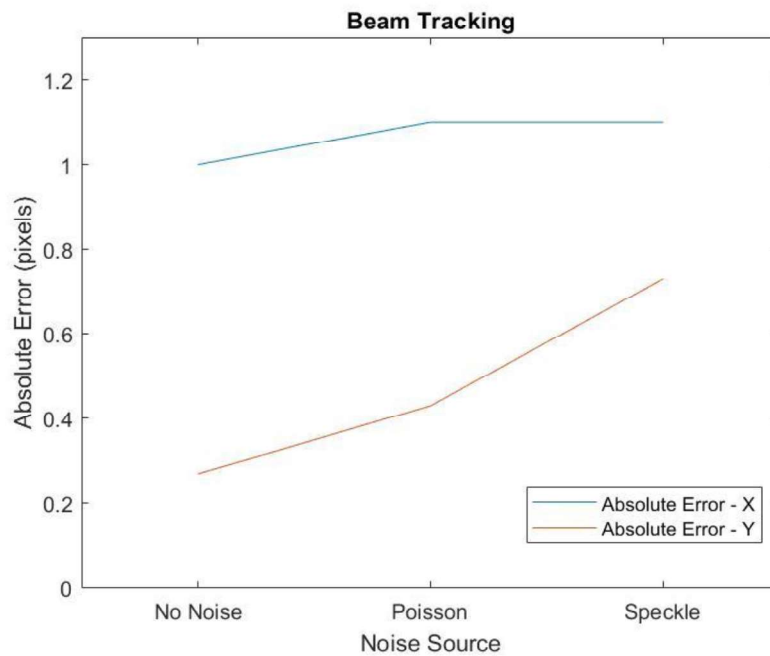
Figure 43: EM Algorithm Beam Shift Tracking

The scene tracking showed similar results to the beam tracking. It showed some success, but it could not deliver perfect shift tracking. These results are shown again in Figure 44. These results could have been expected from the results of the isolated scene update equation testing. Even given the true object and beam shifts, the equation could not perfectly track the input scene shifts. The noiseless simulation performed the best of

60

the noise conditions with 1.07 pixels and 0.17 pixels of absolute error in X and Y, respectively. With Poisson noise added, the scene tracking showed similar performance at 1.27 pixels and 0.20 pixels of absolute error in X and Y, respectively. And finally, after adding speckle and background noise, the scene tracking produced 1.20 pixels and 0.23 pixels of absolute error in X and Y, respectively. Like the beam shift tracking, these results suggest that the scene tracking can handle various noise sources successfully, though not perfectly.

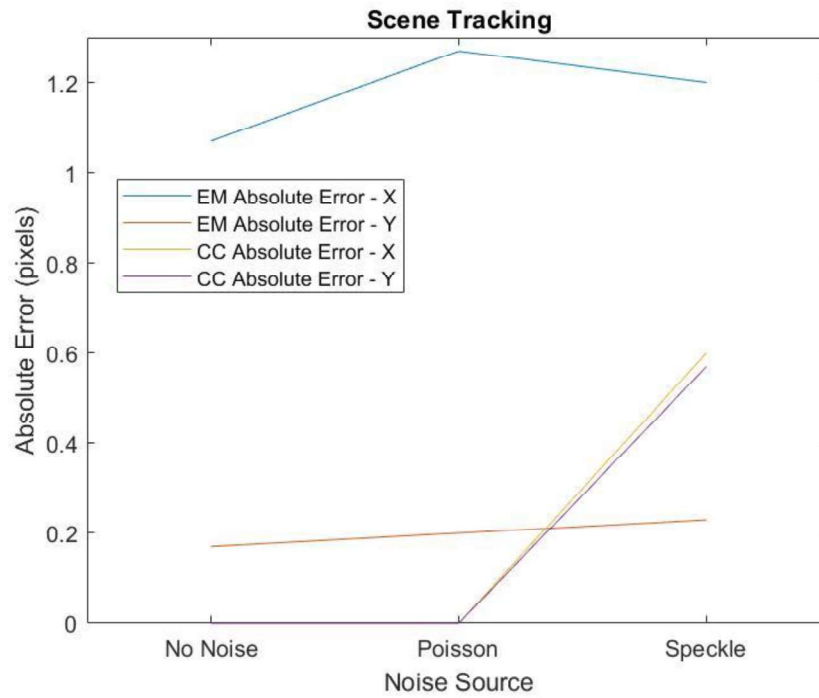**Figure 44: EM vs Cross-Correlation Scene Shift Tracking**

The EM scene tracking has a direct comparison point of cross-correlation to see the success of the algorithm. Under each noise condition, the cross-correlator performed better at tracking the scene shift than the EM algorithm. It was perfect under no noise and Poisson noise conditions where the EM algorithm was not. Under speckle noise, however, the cross-correlator could not perfectly track the input shifts. The cross-correlator produced 0.60 pixels and 0.57 pixels of absolute error in X and Y, respectively; the EM algorithm produced a better estimate in the Y direction under speckle noise. These cross-correlator results show better scene tracking ability than the EM algorithm but show a steep drop off as more noise was added to the simulation.

The final piece to analyze was the object produced from the EM algorithm and the cross-correlation method. These results are shown in Figure 45, below. These results show that the EM object, as expected, produced the least error with no noise and most error with speckle and background noise. More importantly, these results show that the EM optimized object is significantly lower than the cross-correlation object. The cross-correlation object RMSE was 345% higher than the EM optimized object under no noise, 327% higher under Poisson noise, and 232% higher under speckle noise. These numbers suggest that under each noise condition, the EM beam and scene tracking deconvolution algorithm produces a significantly cleaner object than the cross-correlation method.
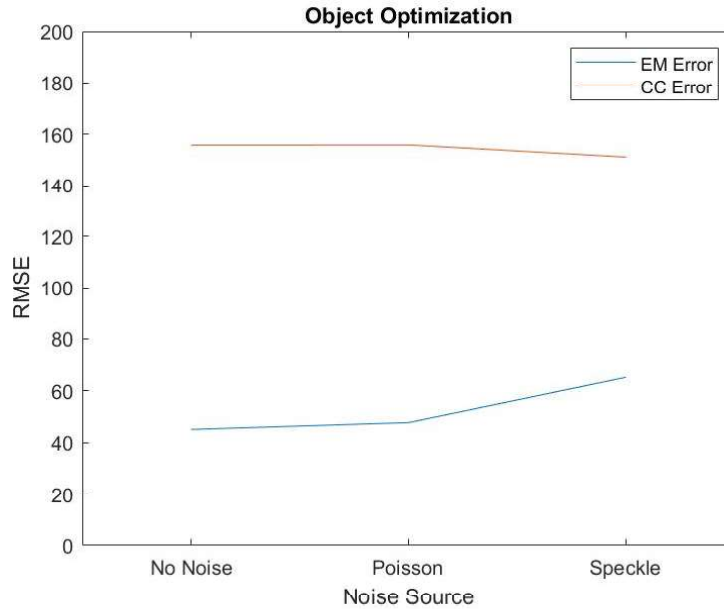
Figure 45: EM vs Cross-Correlation Object Optimization

4.2.2 Hybrid Algorithm Analysis

Beam tracked showed a significant improvement using the hybrid method compared to the EM algorithm. Beam tracking results from both algorithms are shown in Figure 46, below. Looking at each noise source, the hybrid method beam shift tracking performed best under no noise or with Poisson noise. The hybrid approach gave 0.43 pixels and 0.33 pixels of absolute error in X and Y, respectively with no noise present and 0.47 pixels and 0.27 pixels of absolute error in X and Y, respectively with Poisson noise. With each of these noise conditions, the hybrid method clearly outperformed the EM algorithm. Once laser speckle and background noise were added, the hybrid beam shift tracking performed worse. The absolute error in X grew to 1.03 pixels, and the absolute error in Y only grew to 0.97 pixels. These results are noticeably worse than the noiseless and Poisson noise simulations, and no longer exceed the beam tracking abilities of the EM

63

algorithm. Both the EM algorithm and the hybrid algorithm produced similar results. These results suggest that under high noise, the hybrid method is comparable to the EM algorithm at tracking the beam, but with low noise levels the hybrid algorithm is superior.
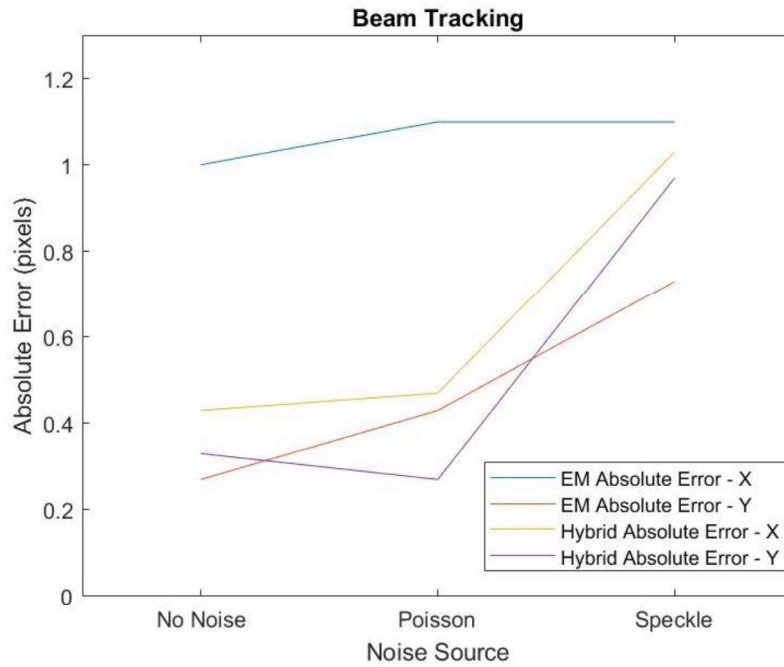
Figure 46: EM vs Hybrid Beam Shift Tracking

Analysis shifted to the scene shift tracking next. Figure 47 shows the scene tracking absolute error from the EM algorithm compared to the hybrid method under each noise condition. Just like the previous simulations, the cross-correlator perfectly estimated the input shifts with no noise and Poisson noise added; these resulted in 0.00 absolute error in each direction. The perfect scene tracking under these noise sources explains the improved beam shift tracking previously reported. The hybrid method was given significantly better scene shift estimates, and that resulted in significantly better beam

64

shift estimates. With speckle and background noise added, the cross-correlation method produced comparable results to the EM algorithm. This also explains why the beam shift tracking was comparable with the hybrid method.
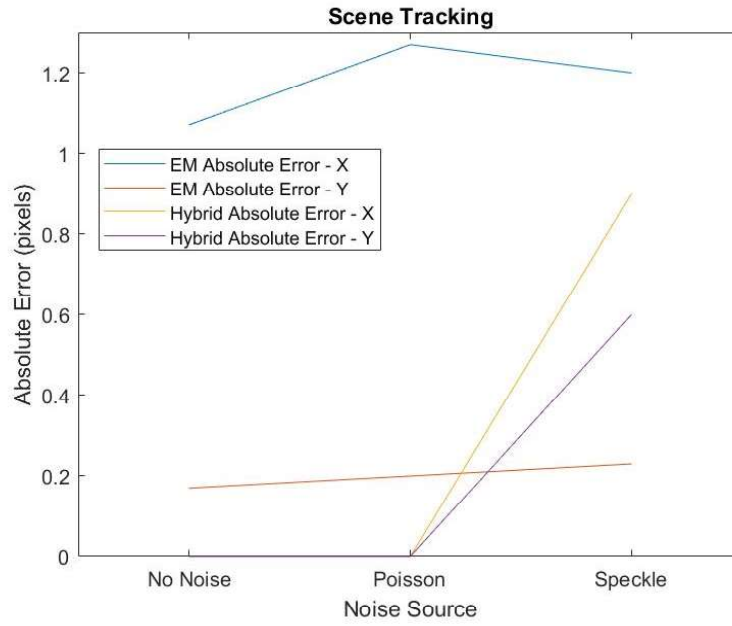
Figure 47: EM vs Hybrid Scene Shift Tracking

The final piece to analyze was the object produced from the hybrid algorithm and compare against the EM algorithm. These RMSE results are shown in Figure 48, below. The EM and hybrid objects are shown side by side for each noise condition in Figure 49. Qualitatively analyzing the images, the hybrid algorithm clearly produces the two cleanest images; the hybrid object under no noise and Poisson noise are both strikingly sharp images of the original target object. Looking at the quantifiable data for these two noise sources, the RMSE calculations confirm that the hybrid is a truly cleaner image with less error.

65

Looking, next, to the speckle noise simulation, the two objects visually look nearly identical. Both images show a strong representation of the original target object, and both images are affected by speckle. Neither algorithm's image seems to be cleaner than the other. The RMSE calculations support this claim. The EM algorithm produced an object with 65.24 RMSE compared to 61.92 RMSE for the hybrid algorithm; both results have very comparable amounts of error. These results follow the trends established with the scene tracking and beam tracking. The cross-correlator produced similar scene tracking results to the EM algorithm at high noise levels, and this caused similar beam tracking results. Given similar beam and scene shift estimates, the hybrid algorithm, predicably, produced a similar quality of optimized object to the EM algorithm.
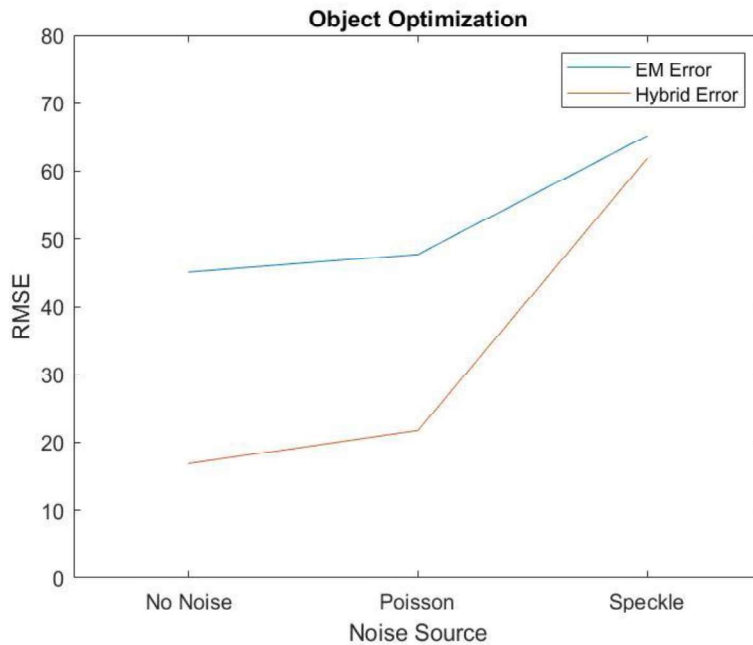
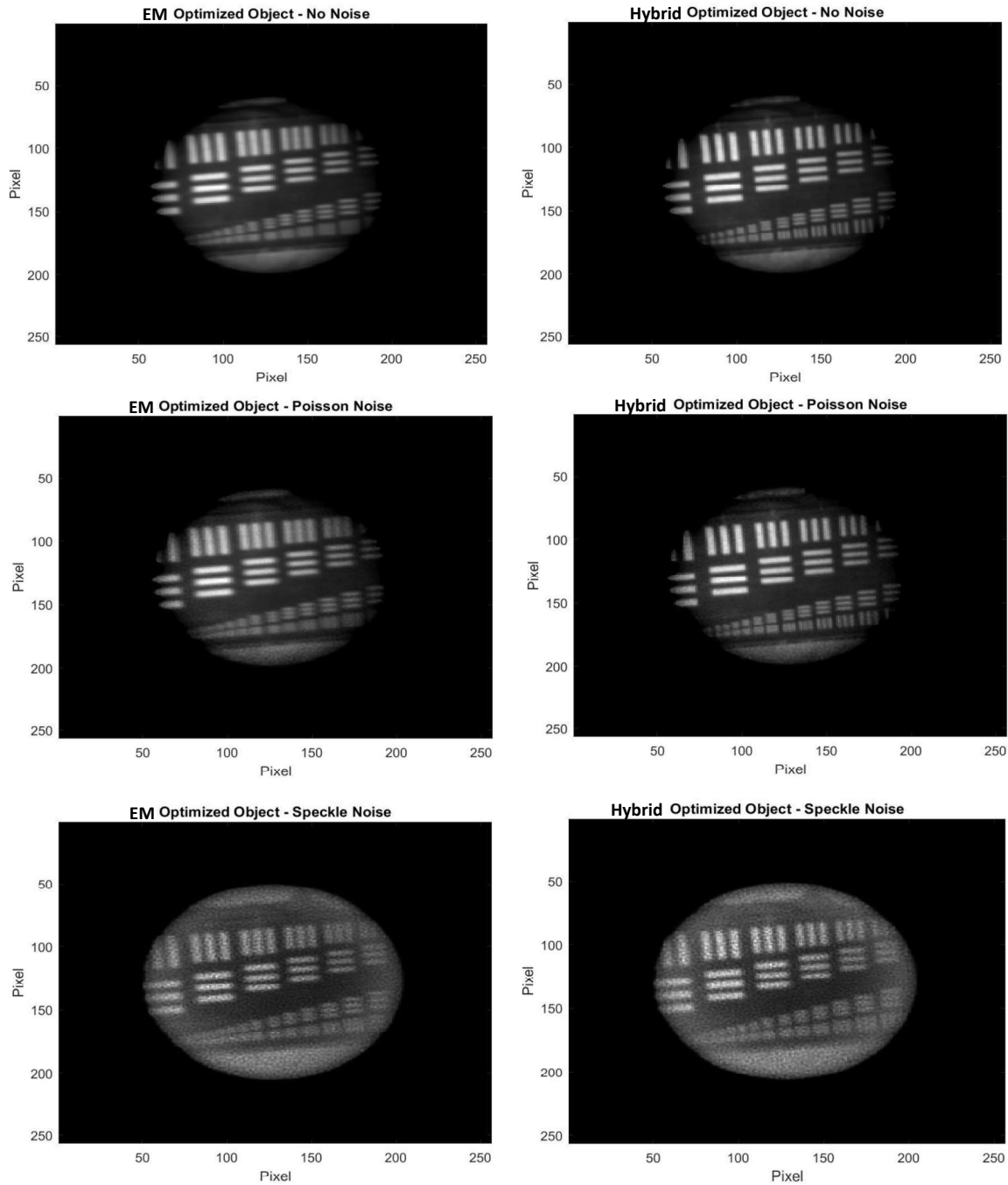

Figure 48: EM vs Hybrid Object Optimization

Figure 49: EM and Hybrid Optimized Objects

V. Conclusions and Recommendations

This chapter will discuss the conclusions gathered from the research and discuss recommendations for future research efforts.

5.1 Conclusions

This research effort developed and tested the beam and scene tracking deconvolution algorithm using the EM algorithm and continued to add to the performance with the hybrid algorithm. Previous research efforts could not perform the beam and scene tracking with the EM derived update equations; these beam and scene shifts were estimated with a block matching approach. Computational advances now allow the beam and scene tracking equations to be implemented entirely with the EM derived update equations, though the scene update equation still cannot estimate the shifts perfectly.

Each component of the beam and scene tracking deconvolution algorithm was isolated and tested individually. The beam shift tracking and object optimization both performed excellently when isolated. The beam shift update equation perfectly tracked each input shift under each noise condition, and the object optimization produced remarkably clean images. However, the scene shift algorithm could not perform perfectly when isolated. This is likely due to computational limitations. The EM algorithm dictates that the algorithm should converge on the true shift, but implementing in simulation found that the computer could not properly estimate the shifts. The EM algorithm shift tracking was outperformed by the cross-correlation algorithm under low noise and performed comparably under high noise.

69

When implementing the entire EM algorithm, the algorithm effectively estimated beam and scene input shifts under various noise conditions. Though the beam shift tracking has no direct comparison point, the EM algorithm's ability to estimate scene shifts could compare directly to the cross-correlation method. The cross-correlation was found to estimate the scene shifts better than the EM algorithm, although under high noise levels the two algorithms produced similar scene tracking abilities. The EM algorithm shined in its ability to produce a clear image of the optimized object. The EM optimized object was much cleaner, visually, than the cross-correlation object, and the RMSE calculations of each object confirmed that there was much less error in the EM algorithm optimized object.

Using the knowledge that the scene shift tracking was performing worse than cross-correlation at estimating input shifts, the research investigated a hybrid algorithm that used cross-correlation and components from the EM algorithm. This hybrid algorithm performed exceptionally under low noise conditions. RMSE calculations show that the optimized objects from the hybrid algorithm had about one third the error of the EM algorithm optimized objects. With laser speckle noise added to the simulation, the cross-correlation only performed comparably to the EM algorithm scene tracking, and the hybrid algorithm performed comparably to the EM algorithm. RMSE calculations confirmed that the hybrid optimized object and EM optimized object had very similar amounts of error.

This research effort has found that a beam and scene tracking deconvolution algorithm can successfully produce cleaner images than using cross-correlation to register and average frames of data under various noise conditions. The EM algorithm produced

70

higher quality objects than the cross-correlation object for each noise condition. Computational limitations affected the algorithm's scene tracking ability, and this in turn affected the overall quality of the output object. The hybrid algorithm worked around the EM scene tracking issues by using cross-correlation estimates and provided exceptional output objects under low noise. Under higher noise, the hybrid algorithm runs into similar scene tracking limitations, and these limitations means the hybrid algorithm outputs similar optimized objects to the EM algorithm.

5.2 Recommendations for Future Research

Though the EM algorithm has proven that it can provide clean images, there are several assumptions and limitations that could be researched further to strengthen the algorithm. This algorithm, as currently implemented, is too slow to provide real-time tracking and object optimization. A research effort to speed up the algorithm, to the point of near real-time object optimization, could prove invaluable and greatly strengthen the utility of the EM algorithm.

This research effort assumed that both the beam shifts and scene shifts are uncorrelated in time, and it simulated them as such. Atmospheric turbulence has been known to be correlated in time. This would result in shifts in the beam that are correlated and, likewise, shifts in the scene that are correlated. This knowledge could be used to improve the beam and scene tracking from frame-to-frame. A research effort moving forward could work to leverage this fact to improve shift tracking and result in a better optimized object.

71

This algorithm's utility has only been proven in simulation. A research effort that collects true test range data and tests the EM and hybrid algorithms with real data could further prove the utility of either algorithm. True test range data could also introduce rotational or scaling differences between frames of the data set; the algorithm was not built to deal with these types of registration challenges. A research effort to deal with these types of registration challenges would also improve the practicality of the algorithm.

This algorithm assumed a fixed and known PSF throughout the simulation testing. It can be difficult to properly gather the atmospheric PSF of laser illuminated imaging systems; a long exposure PSF may not be appropriate. This assumption could be eliminated with use of a blind deconvolution algorithm. This would allow the algorithm to estimate the object and PSF separately at each iteration. This would eliminate the reliance on the assumption of the PSF and would further strengthen the algorithm.

Appendix A

To solve the conditional expectation shown in Equation 9, we define variables d_1, d_2, and d below. Equation 35, Equation 36, and Equation 40 show the relation of these variables to the complete data.

$$d_1 = \tilde{d}_k(x, y, z_0, w_0) \tag{35}$$

$$d_2 = \sum_z^N \sum_w^N \tilde{d}_k(x, y, z, w) - \tilde{d}_k(x, y, z_0, w_0) \tag{36}$$

$$\mathrm{E}[d_1] = m_1 \tag{37}$$

$$E[d_2] = m_2 \tag{38}$$

$$d_1 + d_2 = d \tag{39}$$

$$d = \tilde{d}_k(x, y, z_0, w_0) + \sum_z^N \sum_w^N \tilde{d}_k(x, y, z, w) - \tilde{d}_k(x, y, z_0, w_0) \tag{40}$$

$$= \sum_z^N \sum_w^N \tilde{d}_k(x, y, z, w) = d_k$$

d_1 and d_2 are defined as Poisson random numbers. Their joint probability of is shown below in Equation 41.

$$P(d_1, d_2) = \left(\frac{m_1{}^{d_1} e^{-m_1}}{d_1!} \right) \left(\frac{m_2{}^{d_2} e^{-m_2}}{d_2!} \right) \tag{41}$$

Rearranging Equation 39 and substituting into Equation 41 gives the joint probability of d_1 and d in Equation 43.

73

$$d_2 = d - d_1 \qquad\qquad 42$$

$$P(d_1, d) = \left(\frac{m_1{}^{d_1} e^{-m_1}}{d_1!}\right)\left(\frac{m_2{}^{d-d_1} e^{-m_2}}{(d - d_1)!}\right) \qquad\qquad 43$$

Leveraging the fact that the sum of two Poisson random number is another Poisson random number with the mean being the sum of the means, the PMF of d is shown below.

$$P(d) = \frac{(m_1 + m_2)^d e^{-(m_1+m_2)}}{d!} \qquad\qquad 44$$

Using Equation 39 and Equation 40, Bayes theorem gives the conditional probability of d_1 given d. After some rearranging, it is clear to see that the conditional probability is a binomial PMF, shown in Equation 42, parameterized as shown in the table below. The expected value of a binomial PMF is known to be the product of the number of trials, *n*, and the probability of success, *p*.

$$P(d_1|d) = \frac{P(d_1, d)}{P(d_1, d)} = \frac{\left(\frac{m_1{}^{d_1} e^{-m_1}}{d_1!}\right)\left(\frac{m_2{}^{d-d_1} e^{-m_2}}{(d - d_1)!}\right)}{\frac{(m_1 + m_2)^d e^{-(m_1+m_2)}}{d!}} = \frac{d!}{d_1!(d - d_1)!} \frac{m_1{}^{d_1} m_2{}^{d-d_1} e^{-(m_1+m_2)}}{(m_1 + m_2)^d e^{-(m_1+m_2)}} \qquad 45$$

$$= \frac{d!}{d_1!(d - d_1)!} \frac{m_1{}^{d_1}}{(m_1 + m_2)^{d_1}} \frac{m_2{}^{d-d_1}}{(m_1 + m_2)^{d-d_1}} = \frac{d!}{d_1!(d - d_1)!} \left(\frac{m_1}{m_1 + m_2}\right)^{d_1} \left(\frac{m_2}{m_1 + m_2}\right)^{d-d_1}$$

$$P(n, p) = \frac{n!}{k!(n - k)!} p^k (1 - p)^{n-k} \qquad\qquad 46$$

Table 5: Conditional Expected Value Definitions

Number of Trials	d	$d_k(x, y)$
Number of Successes	d₁	$\tilde{d}_k(x, y, z_0, w_0)$
Probability of Success	$\left(\dfrac{m_1}{m_1 + m_2}\right)$	$\dfrac{o^{old} b(z - \gamma_k{}^{old}, w - \varepsilon_k{}^{old}) h\left(x - z - \alpha_k{}^{old}, y - w - \beta_k{}^{old}\right)}{\sum_z^N \sum_w^N o^{old} b\left(z - \gamma_k^{old}, w - \varepsilon_k^{old}\right) h\left(x - z - a_k^{old}, y - w - \beta_k^{old}\right)}$
Expected Value	$d\left(\dfrac{m_1}{m_1 + m_2}\right)$	$\dfrac{o^{old} b(z - \gamma_k{}^{old}, w - \varepsilon_k{}^{old}) h\left(x - z - \alpha_k{}^{old}, y - w - \beta_k{}^{old}\right) d_k(x, y)}{\sum_z^N \sum_w^N o^{old} b\left(z - \gamma_k^{old}, w - \varepsilon_k^{old}\right) h\left(x - z - a_k^{old}, y - w - \beta_k^{old}\right)}$

Bibliography

[1]   R. J. Noll, "Zernike polynomials and atmospheric turbulence," J. Opt. Soc. Am. 66, pp. 207-211, 1976.

[2]   R. D. Richmond and S. C. Cain, Direct-Detection LADAR Systems, Bellingham WA: SPIE Press, 2010.

[3]   D. Becker, Laser Illuminated Imaging: Multiframe Beam Tilt Tracking and Deconvolution Algorithm, AFIT: Master's thesis, 2013.

[4]   J .W. Goodman, Introduction to Fourier Optics, Greenwood Village CO: Roberts & Company, 2005.

[5]   J. W. Goodman, Statistical Optics, New York NY: John Wiley & Sons Inc, 1985.

[6]   J.C. Dainty, Laser Speckle and Related Phenomena, New York NY: Springer-Verlag Berlin Heidelberg, 1975.

[7]   L. G. Brown, "Survey of Image Registration Techniques,"ACM Computing Surveys, vol. 24, no. 4, pp. 326-378, 1992.

[8]   A. P. Dempster, N. M. Laird and D. B. Rubin, "Maximum likelihood from incomplete data via the em algorithm," *Journal of the Royal Statistical Soc. ,* no. 39, pp. 1-38, 1977.

[9]   G. R. Ayers and J. C. Dainty, "Iterative blind deconvolution method and its applications," Opt. Lett., no. 13, pp. 547-549, 1988.

[10]   D. Dayton, S. Browne, J. Gonglewski, S. Sandven, J. Gallegos and M. Shilko, "Long-range laser illuminated imaging: analysis and experimental demonstrations," *Soc. of Photo-Optical Instrumentation Engineers,* pp. 1001-1009, June 2001.

REPORT DOCUMENTATION PAGE

1. REPORT DATE *(DD-MM-YYYY)*	2. REPORT TYPE	3. DATES COVERED *(From – To)*
04-02-2021	Master's Thesis	September 2019 – March 2021

TITLE AND SUBTITLE	
Laser Illuminated Imaging: Beam and Scene Tracking Deconvolution Algorithm	5a. CONTRACT NUMBER
	5b. GRANT NUMBER
	5c. PROGRAM ELEMENT NUMBER

6. AUTHOR(S)	
Davis, Benjamin W., 1st Lieutenant, USSF	5d. PROJECT NUMBER
	5e. TASK NUMBER
	5f. WORK UNIT NUMBER

7. PERFORMING ORGANIZATION NAMES(S) AND ADDRESS(S)	8. PERFORMING ORGANIZATION REPORT NUMBER
Air Force Institute of Technology Graduate School of Engineering and Management (AFIT/EN) 2950 Hobson Way, Building 640 WPAFB OH 45433-7765	AFIT-ENG-MS-21-M-026

9. SPONSORING/MONITORING AGENCY NAME(S) AND ADDRESS(ES)	10. SPONSOR/MONITOR'S ACRONYM(S)
Intentionally left blank	
	11. SPONSOR/MONITOR'S REPORT NUMBER(S)

12. DISTRIBUTION/AVAILABILITY STATEMENT
   DISTRUBTION STATEMENT A. APPROVED FOR PUBLIC RELEASE; DISTRIBUTION UNLIMITED.

13. SUPPLEMENTARY NOTES
This material is declared a work of the U.S. Government and is not subject to copyright protection in the United States.

14. ABSTRACT
Laser illuminated imaging systems deal with several physical challenges that must be overcome to achieve high-resolution images of the target. Noise sources like background noise, photon counting noise, and laser speckle noise will all greatly affect the imaging system's ability to produce a high-resolution image. An even bigger challenge to laser illuminated imaging systems is atmospheric turbulence and the effect that it will have on the imaging system. The illuminating beam will experience tilt, causing the beam to wander off the center of the target during propagation. The light returning to the detector will similarly be affected by turbulence, and it too will wander off the center of the detector. The effects of tilt will be noticed in a multi-fame data set by the illuminating beam and the object shifting around the frame. This research effort uses expectation maximization to track the beam and scene motion from frame-to-frame along with a deconvolution algorithm to produce a high-resolution image of the target. Components of the expectation maximization beam and scene tracking algorithm will then be used with cross-correlation to create a hybrid algorithm to create exceptionally clear images of the target object.

15. SUBJECT TERMS
Laser Illuminated Imaging, LADAR, Beam Tracking

16. SECURITY CLASSIFICATION OF:			17. LIMITATION OF ABSTRACT	18. NUMBER OF PAGES	19a. NAME OF RESPONSIBLE PERSON
a. REPORT	b. ABSTRACT	c. THIS PAGE			Maj David JR Becker, AFIT/ENG
			UU	88	19b. TELEPHONE NUMBER *(Include area code)*
U	U	U			(937) 255-3636 (david.becker@afit.edu)